JOURNAL OF PETROLOGY | VOLUME 45 | NUMBER 7 | PAGES 1481–1512 | 2004 | DOI: 10.1093/petrology/egh023

Orthopyroxene–Corundum in Mg–Al-rich Granulites from the Oygarden Islands, East Antarctica

N. M. KELLY[1]* AND S. L. HARLEY[2]

[1]DIVISION OF GEOLOGY AND GEOPHYSICS, SCHOOL OF GEOSCIENCES, F05, UNIVERSITY OF SYDNEY, SYDNEY, N.S.W. 2006, AUSTRALIA

[2]SCHOOL OF GEOSCIENCES, UNIVERSITY OF EDINBURGH, GRANT INSTITUTE, KINGS BUILDINGS, EDINBURGH EH9 3JW, UK

RECEIVED MARCH 4, 2003; ACCEPTED FEBRUARY 2, 2004

High-Mg–Al, silica-undersaturated metapelites from the Oygarden Group of islands, East Antarctica, preserve clear evidence for the stable coexistence of the assemblage orthopyroxene + corundum in natural rocks. The quartz-absent metapelite occurs as pods and isolated layers within a high-strain zone related to deformation during the c. *0·93 Ga Rayner Structural Episode. Assemblages that include orthopyroxene, corundum, sapphirine, sillimanite, cordierite, garnet and kornerupine are developed across a pre-existing compositional zoning, leading to contrasting mineral Fe–Mg ratios. The assemblage orthopyroxene–corundum is shown to exist in only a very restricted range of bulk compositions and* P–T *histories. Simplified qualitative FMAS grids have been constructed for kornerupine-absent and -present systems, illustrating MAS terminations and divariant equilibria that help to describe the mineral assemblage and reaction history. Reaction textures that include coronas of sapphirine and sillimanite separating orthopyroxene and corundum, and symplectites of orthopyroxene + sapphirine ± cordierite/plagioclase, orthopyroxene + sillimanite ± cordierite/plagioclase and orthopyroxene + sapphirine + sillimanite embaying garnet, imply a clockwise* P–T–t *evolution. Conditions of* $P > 9$–10 *kbar and* $T \approx 800$–$850^\circ C$ *were attained prior to an initial phase of decompression that was accompanied by heating of up to* $\approx 100^\circ C$. *Peak temperatures of* $T \approx 850$–$900^\circ C$ *were achieved at* $P \approx 9$ *kbar followed by near-isothermal decompression to pressures of* $P \approx 5$ *kbar. This clockwise isothermal decompression path contrasts markedly with anticlockwise isobaric cooling paths recorded elsewhere in the Rayner Complex, and reflects a second phase of orogenesis within the Rayner Structural Episode.*

KEY WORDS: *decompression; kornerupine; orthopyroxene–corundum; reaction textures; sapphirine; symplectite*

INTRODUCTION

Aluminous magnesian gneisses are commonly reported from high-grade metamorphic terranes. Rocks with such compositions are useful for the reconstruction of pressure–temperature–time (*P–T–t*) paths as the mineral assemblages they contain commonly preserve spectacular reaction textures that document segments of *P–T–t* paths (Droop & Bucher-Nurminen, 1984; Windley *et al.*, 1984; Waters, 1986; Droop, 1989). Because of their unusual composition relative to country rocks, these gneisses are also commonly subjected to partial alteration of their margins, thereby creating variations in bulk composition across individual layers. As the position of a particular multi-variant equilibrium in *P–T* space generally depends upon the compositions of the phases involved, an assemblage with given phase compositions may pass through a reaction earlier or later than the same assemblage containing phases with different compositions (e.g. Hensen, 1971). Hence, segments of a *P–T* path can be ascertained by comparing rocks with subtle differences in their bulk compositions, especially variations in Fe–Mg ratios, dependent only on their spatial position with respect to layer boundaries.

Silica-undersaturated metapelites with highly magnesian compositions have been reported from a number of localities in East Antarctica, including MacRobertson Land (Fig. 1; Sheraton *et al.*, 1982; Dunkley *et al.*, 1999), the Napier Complex (Motoyoshi *et al.*, 1995), the Vestfold Hills (Harley, 1993), and the Rauer Group (Harley, 1998*a*). This paper describes a new locality, in the Oygarden Group of islands, East Antarctica, where

*Corresponding author. Present address: School of GeoSciences, University of Edinburgh, Grant Institute, Kings Buildings, Edinburgh EH9 3JW, UK. Telephone: 44-(0)131-650 5885. Fax: 44-(0)131-668 3184. E-mail: Nigel.Kelly@glg.ed.ac.uk

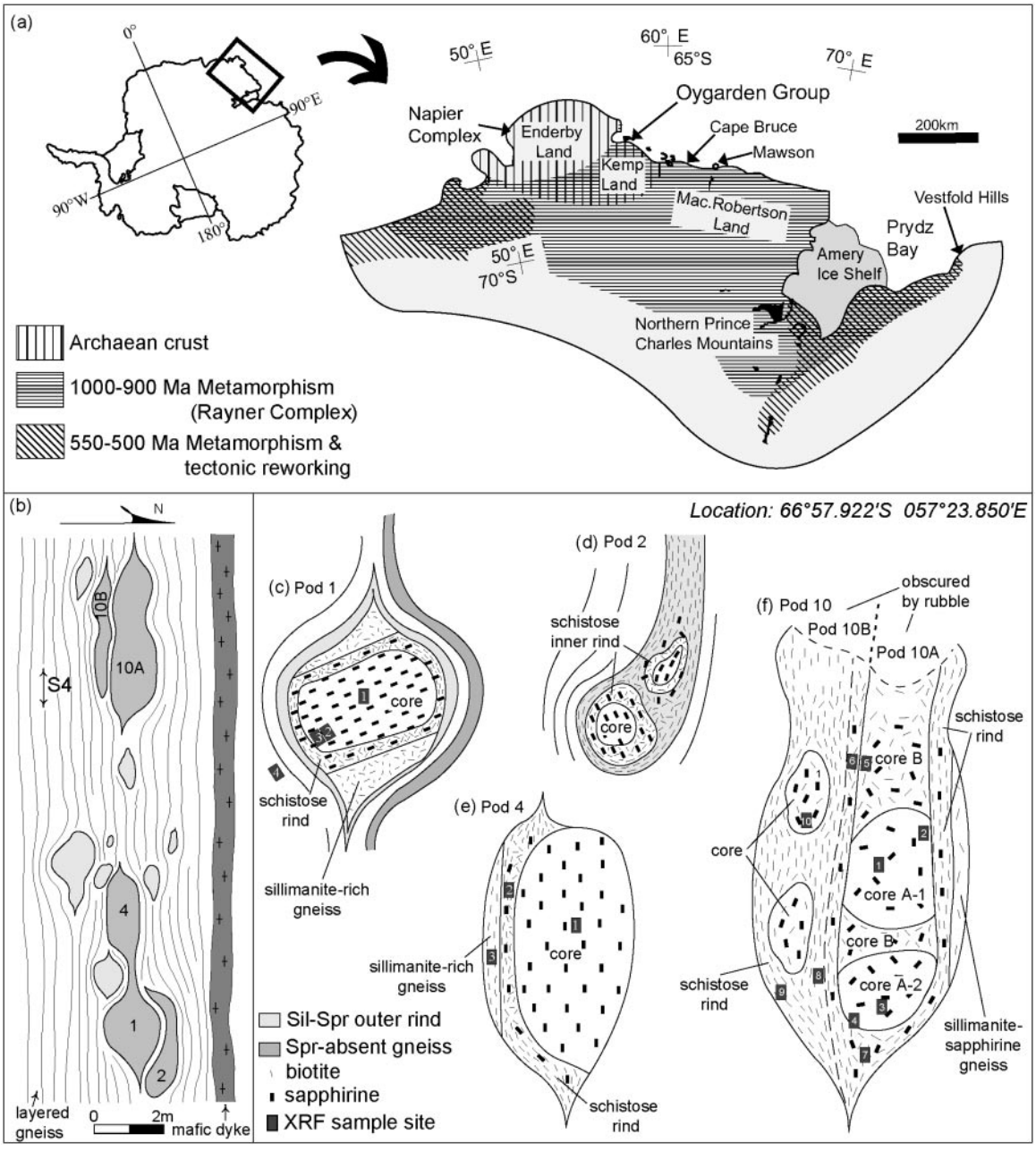

Fig. 1. (a) Location of the Oygarden Islands in Kemp Land, East Antarctica. The map indicates the extent of the Rayner Complex, Rayner tectonic reworking of Archaean crust in Kemp Land, and Neoproterozoic–Cambrian tectonic reworking of Proterozoic crust in Prydz Bay and west of Enderby Land. (b) Sketch map of the outcrop hosting the Si-undersaturated metapelite pods, illustrating the relationship of pods with respect to S_4 layering. (c)–(f) detailed sketches of Pods 1, 2, 4 and 10, illustrating the relationship between compositional zones, internal layering and foliation to external S_4 layering. Shaded boxes with numbers indicate the locations of XRF sample sites, with numbers referring to analyses listed in Supplementary Table 1.

silica-undersaturated metapelitic gneiss preserves assemblages that include orthopyroxene, corundum, sapphirine, kornerupine and garnet, developed within distinct zones across inherited compositional domains. Contrasting mineral compositions and subtly different reaction textures are preserved in the compositionally different zones that are inferred to have formed as a result of a prior metasomatic event. Coexisting orthopyroxene and corundum, which are predicted by theoretical petrogenetic grids to form a stable assemblage under restricted P–T conditions (e.g. Hensen, 1987), but have been loosely inferred to exist in nature (e.g. Windley *et al.*, 1984;

Bertrand *et al.*, 1992; Goscombe, 1992; Kihle & Bucher-Nurminen, 1992), or isolated within extensively developed reaction textures (Ouzegane *et al.*, 2003), are shown more clearly here to have reached textural equilibrium at near-peak *P–T* conditions. These rocks illustrate the importance of subtle variations in bulk composition on resulting reaction products and assemblages, and the preservation of reaction textures and phases. Garnet, sapphirine, orthopyroxene–corundum, and kornerupine-bearing parageneses provide 'snapshots' of a clockwise *P–T–t* evolution that is interpreted to have resulted from prograde thickening of the crust in Kemp Land during the Rayner Structural Episode and decompression from high pressures and temperatures. This *P–T* path contrasts markedly with the dominantly anticlockwise *P–T–t* paths dominated by apparent isobaric cooling, reported elsewhere in the Rayner Complex (Clarke *et al.*, 1989; Fitzsimons & Thost, 1992; Thost & Hensen, 1992; Hand *et al.*, 1994; Nichols, 1995; Boger & White, 2003).

GEOLOGICAL SETTING

The Oygarden Group of islands forms some of the most westerly exposures of the Proterozoic Rayner Complex in Kemp Land (Fig. 1a), which is interpreted to represent Archaean crust that was reworked by the Rayner Structural Episode during the earliest Neoproterozoic (Sheraton & Black, 1983; Clarke, 1987; Sheraton *et al.*, 1987; Grew *et al.*, 1988; Kelly *et al.*, 2002). Lying near the western extremity of this zone of reworking (Sheraton & Black, 1983; Sheraton *et al.*, 1987), the Oygarden Group is considered to have formed part of the Napier Complex from at least *c.* 2·5 Ga, and was tectonically reworked at *c.* 0·93 Ga (Kelly *et al.*, 2002). The Napier Complex, an Archaean ultrahigh-temperature metamorphic terrane, experienced multiple episodes of deformation and metamorphism between *c.* 2·98 Ga and *c.* 2·45 Ga (Sheraton *et al.*, 1987; Harley & Black, 1997).

The Rayner Complex is a composite granulite-facies metamorphic terrane that comprises both reworked Archaean and Proterozoic crust. Orogeny between 1·0 and 0·9 Ga occurred as a result of convergence between an Indo-Napier craton (comprising the Napier Complex and peninsular India) and part of what now constitutes East Antarctica, during the Rayner Structural Episode (RSE: Sandiford & Wilson, 1984; Sheraton *et al.*, 1987). The RSE is characterized by two main phases of deformation that are separated in time by the intrusion of voluminous charnockite in MacRobertson Land and the northern Prince Charles Mountains at 0·98–0·96 Ga (Young & Black, 1991; Kinny *et al.*, 1997; Young *et al.*, 1997; Zhao *et al.*, 1997). The location of the Oygarden Group, which records only the second phase of this deformation (Kelly *et al.*, 2000, 2002), makes this area critical to the understanding of the evolution of this region.

The Oygarden Group of islands was affected by at least five episodes of deformation (D_1–D_5) over a 1·8 Ga period during the Archaean and Proterozoic. The structures in the islands are dominated by those that formed during the RSE: D_3 and D_4. At least two deformation events or sets of structures are recognized to pre-date D_3/D_4. An S_1 gneissosity, defined in part by a migmatitic layering in layered felsic orthogneiss, is identified with confidence only where cut by a homogeneous felsic orthogneiss that intruded during D_1 at *c.* 2·75 Ga (Kelly *et al.*, in preparation). Layered composite orthogneiss, the most abundant lithology, is composed of layers of felsic, intermediate and mafic gneiss that alternate on a centimetre to metre scale. Subordinate lithologies include mafic dykes, calc-silicate gneiss, layered quartz-rich metasediments, quartz-bearing metapelitic gneiss, and silica-undersaturated metapelitic gneiss. D_2 resulted in transposition of S_1 and the homogeneous felsic orthogneiss into S_2 at *c.* 2·45 Ga (Kelly *et al.*, in preparation).

The RSE D_3 deformation is characterized by the effects of east-directed thrusting that occurred at medium- to high-*P* granulite-facies conditions at *c.* 0·93 Ga (Kelly *et al.*, 2002). S_3 assemblages in mafic granulite, including garnet, orthopyroxene, clinopyroxene, plagioclase and quartz, suggest that D_3 occurred at $P \approx 9$–10 kbar and $T \approx 800$–850°C (Kelly *et al.*, 2000). D_4 resulted in a 2–3 km wide extensional shear zone that recrystallized rocks in the south of the island group. D_4 occurred at granulite-facies conditions, similar to those that accompanied D_3 (Kelly *et al.*, 2000). The last event recognized, D_5, is characterized by mylonites and ultramylonites that formed at amphibolite-facies conditions and cut structures that formed during the RSE. Mylonites show a broadly northward sense of transport.

OUTCROP DESCRIPTION AND ASSEMBLAGES

High Mg–Al silica-undersaturated metapelite occurs as more than 15 distinguishable pods and lenses in an outcrop approximately 20 m × 10 m in size within a D_4 high-strain zone (Figs 1b and 2a). The pods form part of a layered sequence that includes garnet-rich felsic and intermediate gneisses, quartz-rich gneiss, and also lenses of quartz-bearing pelitic and semi-pelitic gneiss. S_4 layering envelopes the pods of silica-undersaturated metapelite, but S_4 is not penetratively developed within the pods. Most pods preserve similar assemblage relationships, summarized using four pods (1, 2, 4 and 10) as examples that span the common compositional and textural variations observed (Fig. 1c–f; Table 1). Three main composition/assemblage types occur within the pods,

Table 1: Summary of assemblage and average mineral compositions between and within quartz-absent metapelite pods

		Sapphirine			Orthopyroxene				Cordierite		Garnet		Biotite		Plagioclase		Kornerupine			Sill	Crn	Rct-text
		X_{Mg}	X^*_{Mg}		X_{Mg}	X^*_{Mg}	Al_2O_3		X_{Mg}		X_{Pyp}		X_{Mg}		X_{An}		X_{Mg}	X^*_{Mg}				
Pod 1																						
OG522B/ OG573	core	0·93	0·96	(P, R)	0·89	0·90	5—8·5	P	(0·96—0·97)	R	—	tr, i	0·93	(P, tr)	—	—	—	—	—	(R)	P	A
OG524A/B	edge of core	0·92	0·94	(P, R)	0·87	0·88	4—9·5	P	—	R	0·46—0·70	tr, i	0·90—0·91	(P)	—	—	—	—	—	R	P	(A, B)
OG522A	core—rind overlap	0·91	0·93	(P, R)	0·86	0·86	6—9	P	0·94—0·95	R	0·67—0·70	tr, i	0·88—0·90	P	—	—	—	—	—	R	P	(A, B)
OG571	schistose rind	0·90	0·93	(P, R)	0·86	0·86	6—8	P	0·94—0·95	R	0·70	tr, i	0·85—0·87	P	0·30	(R)	—	—	—	(?P),R	P	(A, B)
OG570	Sil-rich gneiss	—	—	—	0·84	0·87	6—8	P	0·94	R	0·70	tr, i	0·87	(P)	0·29	(R)	—	—	—	(P, R)	—	—
Pod 2																						
OG566	core	0·88—0·9	0·93	P	0·85	0·86	6·7—8·7	P	—		0·66	tr, i	0·88	P, tr	—	—	0·90	0·94	P	(R)	(P), incl	A
OG567A/B	schistose rind	0·89	0·93	P, R	0·84	0·86	6—8·9	P	0·94	R	0·61—0·67	P	0·87	P	—	—	0·90	0·93	(P, R)	(?P), R	(P), incl	A,B,G,H
Pod 4																						
OG575	core	0·94	0·97	P, R	0·91	0·93	5·5—8·0	P	—		—	tr, i	—	—	—	—	—	—	—	(R)	P	A
OG576	schistose rind	0·92	0·96	P, R	0·87	0·89	6·0—9·2	P	—	R	0·70	i	0·90—0·91	P	—	—	—	—	—	(?P), R	—	
OG577	Sil-rich gneiss	0·92	0·93	R	0·86	0·88	4·5—9	P	0·94—0·95	R	0·66	P	0·89—0·90	(P)	—	—	—	—	—	P, R	—	FI
Pod 10																						
OG587	Core (a-1)	0·95	0·97	P, R	0·91	0·92	3·3—8	P, R	—	R	0·74	tr, i	0·94	(P)	0·49	(R)	—	—	—	R	—	C, D, F
OG588	Core (a-2)	0·92	0·94	P, R	0·87	0·87	6·5—8·5	P, R	—	R	0·67	tr, i	0·90	(P)	0·48	(R)	—	—	—	R	—	C, D, F
OG584/ OG580	Core (a) adj. rind	0·91	0·93	P, R	0·89	0·87	5·0—9·0	P, R	0·85	R	0·64—0·66	(P)	0·89	P	0·47—0·51	(R)	—	—	—	R	—	C
OG585	Core (b) adj. rind	0·90	0·93	P, R	0·85	0·87	6·0—8·5	P, R	—	R	0·62	(P)	0·89	P	0·40	(R)	—	—	—	R	—	C, D
OG581	schistose rind	—	—	—	0·81	0·82	3·5—7·5	P, R	0·93	R	0·58	P	0·85	P	0·31	(R)	—	—	—	R	—	D, E
OG586	Sil—Spr gneiss	0·90	0·95	R	0·84	0·89	6—8·8	P, R	—	R	0·63	P	0·86—0·89	(P)	0·55	(R)	—	—	—	R	—	C
Pod 12																						
	core	—	—	P	—	—	—	—	—	—	—	—	—	(P)	—	—	—	—	—	(R)	—	F
	schistose rind	—	—	P, R	—	—	—	—	—	—	—	P	—	P	—	—	—	—	—	(?P), R	—	—

All assemblages include rutile, which is the only Fe—Ti oxide present in the samples; P, peak mineral; R, retrograde mineral; ( ), minor occurrence; tr, trace occurrence; i, inclusion; $X_{Mg} = Mg/(Fe_{tot} + Mg)$; $X^*_{Mg} = Mg/(Fe^{2+} + Mg)$; $X_{Pyp} = Mg/(Mg + Fe_{tot} + Mn + Ca)$; $X_{An} = Ca/(Ca + Na + K)$. Reactions: A, Opx + Crn = Spr + Sil; B, Opx + Sil = Spr + Crd; C, Grt = Opx + Spr + Crd/Plag; D, Grt = Opx + Sil + Crd/Plag; E, Grt + Qtz = Opx + Plag; F, Grt = Opx + Sil + Spr; G, Grt + Spr = Opx + Krn; H, Opx + Sil + Spr = Krn. Abbreviations are after Kretz (1983).

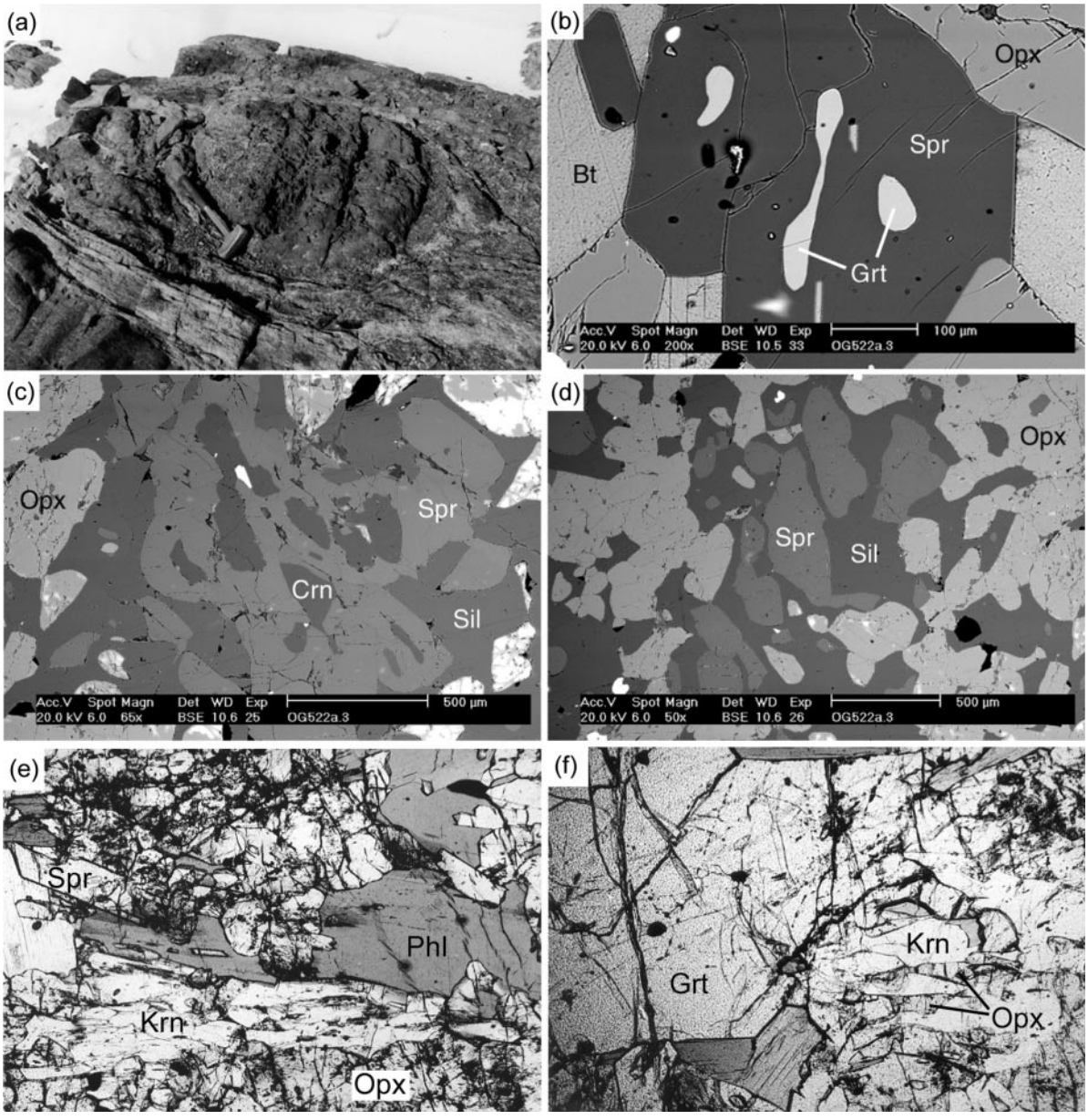

Fig. 2. (a) Outcrop photograph of Opx–Spr–Crn-bearing metapelite (Pod 1), enveloped by S_4 layering. (Geological hammer for scale is 40 cm in length.) (b) Back-scattered electron (BSE) image of garnet inclusions in S_3 sapphirine (sample OG522A, Pod 1; scale bar represents 100 µm). (c) BSE image of relic corundum grains within an extensive growth of sapphirine and sillimanite (scale bar represents 500 µm). (d) BSE image of a sapphirine–sillimanite intergrowth in orthopyroxene from the transition zone in Pod 1 (sample OG522A). The sapphirine is interpreted to have completely replaced corundum, and sillimanite is beginning to dominate the texture (scale bar represents 500 µm). (e) Plane-polarized light photomicrograph of S_3 kornerupine, sapphirine, phlogopite and orthopyroxene (sample OG566; width of field of view is 4 mm). (f) Plane-polarized light photomicrograph of an orthopyroxene–kornerupine intergrowth embaying a garnet porphyroblast (sample OG566; width of field of view is 4 mm).

with other subordinate compositions and assemblages occurring as layers bounding or enveloping the pods. These main types are: (1) garnet-poor, where garnet occurs only as fine-grained and volumetrically insignificant inclusions in sapphirine or sillimanite; (2) garnet-rich, where garnet is abundant in outer zones of pods; (3) kornerupine-bearing, which may or may not contain abundant garnet. Nearly all pods preserve an assemblage zoning pattern characterized by anhydrous cores dominated by coarse-grained orthopyroxene and sapphirine with a transition zone into 10–15 cm wide, phlogopite-rich schistose rinds. The anhydrous cores commonly

preserve a foliation (S_3) that is oblique to the enveloping S_4 layering and foliation developed in schistose rinds (e.g. Fig. 1c). The orientation of S_3 is not consistent between pods, which is interpreted to reflect variable rotation of pods during D_4 deformation.

Garnet-poor (quartz-absent) assemblages

The core assemblages in garnet-poor pods (Pods 1 and 4; Table 1) are composed of S_3 sapphirine, orthopyroxene and corundum, with or without minor sillimanite, cordierite and phlogopite. Rutile also occurs as part of S_3, and is the only Fe–Ti oxide present in any zone. Garnet is low in abundance and occurs only as fine-grained inclusions (less than 0·5 mm; Fig. 2b) in elongate sapphirine grains (Pod 1), and is absent from the core of Pod 4. Sapphirine commonly occurs as elongate grains and clusters of grains up to 2 cm in length, and may also form elongate 'cuneiform' grains in orthopyroxene. In Pod 4, orthopyroxene may occur as large (up to 5–6 mm), elongate grains with lobate and eroded grain boundaries, and abundant fine-grained rutile inclusions. Sapphirine may form large xenoblasts that contain inclusions of rounded orthopyroxene. Corundum is scattered in this pod and is not confined to the core region. Where corundum occurs it is always separated from orthopyroxene by a thin (up to 0·3 mm), but complete, corona of sapphirine (Fig. 3a). Importantly, the grain size of sapphirine in the coronas is appreciably smaller than that of the orthopyroxene and corundum grains that they separate. Sillimanite may rarely form an outer, continuous or discontinuous rim between sapphirine and orthopyroxene (similar to Fig. 3b), and can appear to embay these minerals. Cordierite is rare, forming narrow rims between sillimanite and orthopyroxene and inclusions in orthopyroxene. Rare phlogopite occurs as inclusions in, or along grain boundaries of orthopyroxene.

A two-stage transition zone occurs between the core and schistose rind. The first stage involves a marked increase in sillimanite (Fig. 2c and d), which interfingers with orthopyroxene and sapphirine, and a minor increase in phlogopite content (Fig. 4). In some local domains orthopyroxene and sapphirine form rounded inclusions in larger sillimanite grains. The second stage is characterized by a marked increase in phlogopite and cordierite. Corundum is present throughout the transition zone, and is commonly separated from orthopyroxene by double coronas of sapphirine and sillimanite (Fig. 3b). A schistose rind up to 15 cm in width occurs on all pods (Fig. 1c–f), and in garnet-poor types is characterized by a smaller grain size and lower abundance of rutile compared with the core. Sillimanite-rich domains occur; however, cordierite-rich domains are predominant. Sapphirine and orthopyroxene both appear to be in overall textural equilibrium with other phases, but locally may be partially embayed by sillimanite or cordierite. Rarely, sapphirine may contain inclusions of phlogopite, orthopyroxene, corundum and garnet. Corundum is surrounded by coronas of sapphirine and either sillimanite or cordierite (Fig. 3c). Proximal to the margin of the schistose rind, phlogopite and sapphirine are foliated parallel to the pod margin and to S_4 (Fig. 1b and c).

Garnet-rich (quartz-absent) assemblages

These assemblages (summarized here using Pod 10 as an example; Fig. 1f; Table 1) show similar assemblage and zoning patterns to other pods but are comparatively garnet-rich, contain plagioclase and have no corundum. Core assemblages have higher abundances of cordierite, sillimanite and phlogopite compared with other pods, which is interpreted to reflect more intense metasomatic alteration prior to the development of the assemblages. The core assemblages may preserve cordierite-poor domains that contain sub-idioblastic, tabular sapphirine grains that appear needle-like in cross-section. Cordierite-rich domains that surround cordierite-poor areas contain large poikiloblastic sapphirine (>2 mm) and sillimanite intergrown with, or containing inclusions of, orthopyroxene, cordierite and garnet. Cordierite occurs as rims on and interfingering with orthopyroxene, sapphirine and sillimanite. An outer core, with higher abundance of phlogopite and sillimanite, may envelop the main core, and commonly contains interstitial patches of plagioclase. The transition zone differs from other pods in its preservation of garnet porphyroblasts (up to 1 mm) and higher modal abundance of cordierite. Intergrowths of tabular sapphirine with orthopyroxene in this zone may be partially replaced by coarse-grained cordierite, which may also embay coarse-grained orthopyroxene, sapphirine and sillimanite. Garnet is present as inclusions in sapphirine, orthopyroxene and cordierite.

The schistose rind is relatively garnet-rich compared with other pods. However, garnet-poor compositional sub-domains do occur that are similar to schistose rinds in garnet-poor rocks. Garnet-rich domains contain coarse-grained garnet, orthopyroxene and sillimanite, with or without sapphirine. In one sample (OG581) a quartz vein (approximately 2 mm in width) cuts the quartz-absent rock, armoured from the latter by a 0·25–0·5 mm wide moat of orthopyroxene. A zone of coarse-grained plagioclase up to 3 mm in width separates this moat from coarse-grained garnet in the quartz-absent host, and is commonly rimmed by cordierite. Rare symplectites of orthopyroxene and cordierite may also occur adjacent to garnet grains. Approximately >5 mm from the quartz vein, garnet is surrounded and embayed by symplectites of orthopyroxene + sillimanite, with or without plagioclase and cordierite (Fig. 3d). In sub-domains ≈2–3 cm away from the large garnet grains described above, the assemblage is composed of a coarse-grained

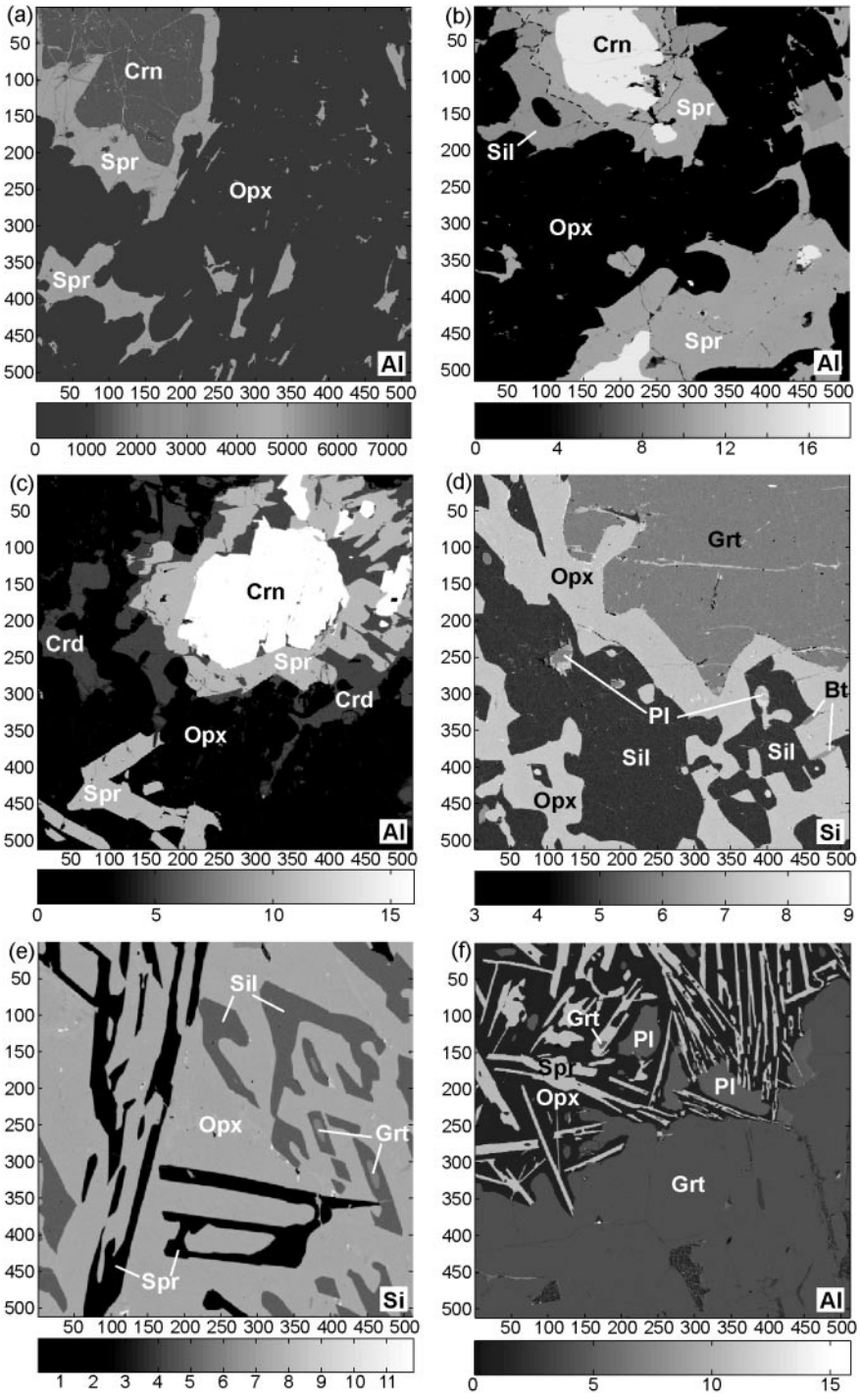

Fig. 3. Grey-scale X-ray intensity maps (512 × 512 pixels) for selected textures illustrating variation in elemental abundance. All maps except (a) have been recalculated to cations per 24 oxygens; (a) is a raw count intensity map. (a) Al map from Pod 1, edge of core (sample OG524A): narrow corona of sapphirine separating corundum from orthopyroxene (analysis step-size 4 μm). (b) Al map from Pod 1, transition zone (sample OG524A): corona of sapphirine and sillimanite between corundum and orthopyroxene (top left of map), and coarse sapphirine developed around corundum (bottom of map; analysis step-size 4 μm). (c) Al map from Pod 1, schistose rind (sample OG524B): intergrowth of sapphirine and cordierite in a corona between corundum and orthopyroxene. Sapphirine also occurs as elongate grains (analysis step-size 4 μm). (d) Si map from Pod 10, schistose rind (sample OG581): garnet surrounded by an intergrowth of orthopyroxene, sillimanite and plagioclase (analysis step-size 3 μm). (e) Si map from Pod 4, sillimanite-rich gneiss (sample OG577): symplectite of orthopyroxene, sillimanite and sapphirine, with garnet inclusions in sillimanite (analysis step-size 2 μm). (f) Al map from Pod 10, sillimanite–sapphirine gneiss (sample OG582A): garnet surrounded by a symplectite of orthopyroxene, sapphirine and plagioclase (analysis step-size 4 μm).

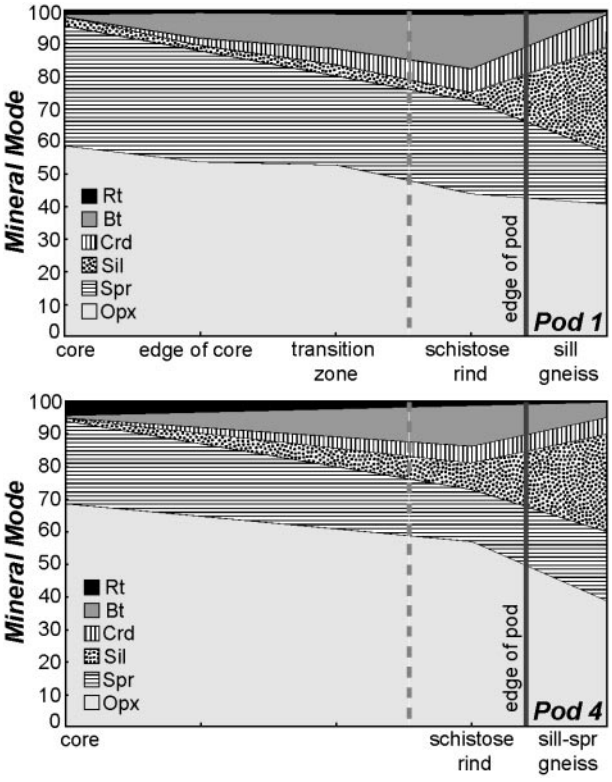

Fig. 4. Variation in mineral modal percentages across two selected pods (1 and 4), illustrating the rimward decreases in modal abundances of orthopyroxene, sapphirine and rutile, and increases in sillimanite, cordierite and biotite. (Figure not to scale; see Fig. 1b for true distances.)

intergrowth of sillimanite and orthopyroxene, and medium-grained garnet.

Kornerupine-bearing (quartz-absent) assemblages

Kornerupine has been identified in a single pod (Pod 2) within the suite (Fig. 1d). This pod preserves core and transition assemblages similar to those in garnet-poor rocks. However, the schistose rind has higher garnet abundance compared with garnet-poor assemblages described above. All zones are kornerupine-bearing. Kornerupine occurs in the core assemblage as elongate grains, generally <1 mm in length, that define S_3 (Fig. 2e). Kornerupine may contain inclusions of garnet and corundum, be overgrown by orthopyroxene, and occur as inclusions in S_3 sapphirine. Corundum inclusions are separated from kornerupine and orthopyroxene by coronas of sapphirine. Garnet occurs as fine-grained inclusions in sapphirine, whereas phlogopite may contain inclusions of sapphirine. In the schistose rind sapphirine, sillimanite, phlogopite and kornerupine surround coarse-grained (up to 2 mm) garnet, which may be embayed by kornerupine and orthopyroxene intergrowths (Fig. 2f). Garnet may also occur as coarse-grained inclusions in sapphirine, sillimanite and orthopyroxene. Sapphirine may contain inclusions of kornerupine. Adjacent to the core, the rind assemblage is aligned parallel to S_3, but closer to the pod margin, sapphirine, sillimanite, phlogopite and kornerupine are parallel to S_4.

Other quartz-absent assemblages

Present in the outcrop are compositionally distinct layers that may occur adjacent to the schistose rind on a single side of a pod (e.g. Pods 4 and 10), on both sides (Pod 1) or completely surrounding the pod (Pod 2; Fig. 1). In Pod 1 (Fig. 1c), the straight boundary between the schistose rind and a sillimanite-rich gneiss is parallel to S_3 preserved in the core of the pod, and oblique to the enveloping S_4. It is possible that these compositional layers reflect a primary compositional layering or are the result of metasomatic alteration of a more homogeneous protolith prior to D_4. Sillimanite-rich gneiss (Pods 1 and 4) contains an assemblage composed of randomly oriented, coarse-grained orthopyroxene, sillimanite, phlogopite, cordierite and plagioclase, with minor garnet. Patchy phlogopite and sillimanite may define S_4 close to the pod margin, but away from the pod margin sillimanite may occur as radiating aggregates. Sillimanite may be separated from orthopyroxene by medium- to coarse-grained rims of cordierite, which contain inclusions of phlogopite, sillimanite and orthopyroxene. In Pod 4 the sillimanite-rich gneiss preserves spectacular 'cuneiform' intergrowths of sillimanite and sapphirine in orthopyroxene (Fig. 3e). Garnet occurs as inclusions in sapphirine and sillimanite. Sillimanite–sapphirine gneiss, occurring as a distinct layer or outer rind (Pods 1, 2, 10; Table 1), is composed of coarse-grained sillimanite, sapphirine, orthopyroxene, phlogopite and garnet. In Pod 10, sillimanite-absent domains occur where large garnet porphyroblasts (2–4 mm) are embayed by symplectites of orthopyroxene and random, 'spinifex-like' arrays of tabular sapphirine, with or without plagioclase (Fig. 3f). Smaller garnet grains may also occur with coarse-grained orthopyroxene, sapphirine and plagioclase, and as inclusions in elongate sapphirine grains. Phlogopite is rare.

Quartz-bearing metapelite

Quartz-bearing metapelitic gneiss associated with quartz-absent rocks commonly preserves similar assemblages and reaction textures. The rocks predominantly preserve a coarse-grained S_4 assemblage of orthopyroxene, garnet and sillimanite, with medium-grained biotite, plagioclase, quartz and rutile, with or without K-feldspar. In more leucocratic samples, S_4 is defined by alternating garnet–orthopyroxene-rich and quartzo-feldspathic domains.

In some samples coarse-grained plagioclase (2–3 mm) occurs in leucosomes and contains fine-grained vermicular inclusions of quartz and K-feldspar. In leucocratic domains, cordierite occurs as large grains, but also forms part of symplectites with orthopyroxene that separate garnet and biotite, or biotite and quartz.

MINERAL CHEMISTRY OF QUARTZ-ABSENT METAPELITE

Electron microprobe point analyses and X-ray intensity maps were collected using the Cameca Camebax SX-50 electron microprobe housed at the Electron Microscope Unit, University of New South Wales, operating with an accelerating voltage of 15 kV, beam current of 20 nA, beam width of 1–5 μm and PAP data reduction software supplied by the manufacturer and described by Pouchou & Pichoir (1984). X-ray intensity maps were collected with a 1–3 μm beam size and count times of 300 ms at each point. X-ray intensity data (Figs 3 and 6) were reprocessed to display weight percent oxide values and molecular proportions following the method described by Clarke *et al.* (2001), which uses the computer software Matlab incorporating a matrix correction algorithm based on the empirical α-factor approach of Bence & Albee (1968). Additional samples were analysed at the Department of Geology and Geophysics, University of Edinburgh, using a Cameca Camebax Microbeam electron microprobe operating at an accelerating voltage of 20 kV and beam current of 25 nA. No systematic differences were detected in compositions between minerals analysed in Edinburgh and Sydney. Microprobe analyses representing the range of mineral compositions are presented in Table 2. Back-scattered electron images (Fig. 2) were collected at the University of Edinburgh, using a Phillips XL30 scanning electron microscope operating at an accelerating voltage of 20 kV. In addition to analysis by electron microprobe, kornerupine was analysed by secondary ion mass spectrometry (SIMS) using the Cameca IMS-4f at the Department of Geology and Geophysics, University of Edinburgh, following methods outlined in detail by Hinton (1995). A primary $^{16}O^-$ beam at ≈8 nA was accelerated through 10 kV and positive secondary ions drawn at a 75 V offset. ^{1}H, ^{7}Li, ^{9}Be and ^{11}B, and a suite of other major and trace elements (Table 3), were analysed as isotopic ratios referenced against ^{28}Si, and ppm concentrations of elements calculated by reference to ion yields determined using the NIST (SRM610) glass standard.

Across each pod the X_{Mg} values [= Mg/(Mg + Fe)] preserved by all ferromagnesian minerals gradually decrease from core domains to the schistose rinds (Fig. 5; Table 1), but are variable in sillimanite-rich gneiss and sillimanite–sapphirine gneiss. This decrease in mineral X_{Mg} correlates with an increase in phlogopite abundance in the rinds. Relative X_{Mg} values [$Mg/(Mg + Fe^{tot})$] between minerals occur in the same order in nearly all pods and zones, with cordierite > sapphirine > phlogopite > orthopyroxene > garnet. When considering Fe^{3+}, X^*_{Mg} [$Mg/(Mg + Fe^{2+})$] of sapphirine may in some cases be equal to that of cordierite, and in rare circumstances phlogopite may be slightly more magnesian than sapphirine. Where present, kornerupine X_{Mg} may be less than sapphirine (Pod 2 core zone) or intermediate between sapphirine and cordierite values. However, when compositions are recalculated to consider Fe^{3+}, kornerupine may become more magnesian than sapphirine (Pod 2 core zone) or marginally less magnesian (Pod 2 schistose rind).

Sapphirine

Compositional zoning of sapphirine is characterized by a systematic decrease in X_{Mg} [= $Mg/(Mg + Fe^{tot})$] in grains with proximity to the edge of pods. Pod 1 core compositions have $X_{Mg} \approx 0{\cdot}93$–$0{\cdot}94$, and decrease to $X_{Mg} \approx 0{\cdot}90$–$0{\cdot}92$ in the schistose rinds (Table 1). Pod 2 sapphirine has slightly lower X_{Mg} values (0·91–0·89). Sapphirine from the sillimanite-rich and sillimanite–sapphirine gneiss also commonly has lower X_{Mg} compared with the schistose rinds. Sapphirine in all pods and zones has between 4·5 and 4·3 Al cations (per 10 oxygens) and shows a rimward increase in Al and decrease in Si. Sapphirine rims adjacent to corundum or sillimanite are commonly more enriched in Al when compared with rims adjacent to orthopyroxene, garnet or biotite. Compositions approach a stoichiometric ratio of 7:9:3 (Mg:Al:Si; where Al = 4·5, Si = 0·75 cations p.f.u.), with cores (higher Si) trending approximately towards 33% of a 2:2:1 composition (Al = 4, Si = 1 cations p.f.u.; Fig. 7a). Analysed compositions lie off the ideal Tschermak's substitution line ($AlAlSi_{-1}Mg_{-1}$) indicating a proportion of Fe^{3+} in total Fe. Fe^{3+} concentration, calculated by assuming 14 cations per 20 oxygens and using the structural formula $M_7(M)O_2[T_6O_{18}]$ (after Moore, 1969), where $Fe^{3+} = Al^{VI} - Al^{IV}$ [$Al^{VI} = 6 - (Si + Ti)$; $Al^{IV} = Al^{tot} - Al^{VI}$], ranges between 0·05 and 0·18 cations p.f.u. (average 0·10 ± 0·3). These values show no consistent trend within or between pods, or in relation to the Tschermak's substitution. Fe^{3+}/Fe^{total} ranges between 0·14 and 0·48, but averages 0·35 ± 0·04. By taking Fe^{3+} into account X_{Mg} values increase by between 0·02 and 0·05 units (Tables 1 and 2a).

Orthopyroxene

Individual grains are rarely zoned with respect to X_{Mg} and values within domains are relatively uniform. However, rare grains preserve weak increases in X_{Mg} at rims

Table 2a: Representative electron microprobe analyses of minerals in typical quartz-absent metapelites

	Sapphirine				Orthopyroxene			Kornerupine		
Pod/zone:	10 (core A)	10 (core A)	2 (rind)	2 (rind)	10 (core A)	10 (core A)	1 (core–rind)	2 (core)	2 (rind)	2 (rind)
Sample:	OG588	OG588	OG567A	OG567A	OG588	OG588	OG524A	OG566	OG567A	OG567B
Analysis:	3.31 core	3.32 adj Opx	1.14 core	1.17 adj Opx	traverse	traverse	5.3 in Spr	1.20 Krn core	6.20 Krn	1.1 Krn core
wt %										
SiO_2	13·555	12·819	13·930	12·903	53·479	56·158	51·362	29·738	29·343	29·484
TiO_2	0·000	0·009	0·059	0·062	0·065	0·064	0·000	0·131	0·164	0·193
Al_2O_3	63·424	64·936	62·594	64·209	7·610	3·307	9·531	47·442	47·143	46·626
Cr_2O_3	0·079	0·127	0·371	0·541	0·004	0·000	0·029	0·053	0·092	0·061
FeO	1·905	1·933	4·612	4·492	5·176	5·735	9·601	3·159	3·284	3·885
MnO	0·016	0·039	0·070	0·000	0·031	0·020	0·047	0·008	0·008	0·047
MgO	20·168	19·614	19·551	19·201	32·859	34·589	29·639	17·96	18·787	17·989
CaO	0·020	0·011	0·000	0·005	0·063	0·058	0·067	0·072	0·044	0·04
Na_2O	0·004	0·000	0·006	0·017	0·000	0·000	0·033	0·052	0·089	0·112
K_2O	0·013	0·001	0·000	0·004	0·004	0·002	0·008	0·008	0·000	0·002
B_2O_3								0·940	0·940	0·940
Total	99·184	99·489	101·193	101·434	99·291	99·933	100·317	99·563	99·894	99·379
No. ox	20	20	20	20	6	6	6	21·5	21·5	21·5
Cations p.f.u.										
Si	1·585	1·495	1·618	1·496	1·845	1·929	1·792	3·692	3·640	3·685
Ti	0·000	0·001	0·005	0·005	0·002	0·002	0·000	0·012	0·015	0·018
Al	8·742	8·926	8·574	8·777	0·310	0·134	0·392	6·944	6·895	6·870
Cr	0·007	0·012	0·034	0·050	0·000	0·000	0·001	0·005	0·009	0·006
Fe^{2+}	0·098	0·106	0·269	0·216	0·149	0·160	0·256	0·213	0·221	0·264
Fe^{3+}	0·088	0·083	0·179	0·220	0·000	0·005	0·024	0·115	0·119	0·142
Mn	0·002	0·004	0·007	0·000	0·001	0·001	0·001	0·001	0·001	0·005
Mg	3·514	3·408	3·385	3·318	1·689	1·771	1·541	3·323	3·474	3·351
Ca	0·003	0·001	0·000	0·001	0·002	0·002	0·003	0·010	0·006	0·005
Na	0·001	0·000	0·001	0·004	0·000	0·000	0·002	0·013	0·021	0·027
K	0·002	0·000	0·000	0·001	0·000	0·000	0·000	0·001	0·000	0·000
B								0·201	0·201	0·203
Total	14·042	14·036	14·073	14·087	3·999	4·003	4·013	14·530	14·604	14·576
X_{Mg}	0·950	0·948	0·883	0·884	0·919	0·915	0·846	0·910	0·911	0·892
Fe^{3+}/Fe^{tot}	0·473	0·439	0·399	0·504	0·000	0·031	0·085	0·35[1]	0·35[1]	0·35[1]
X^*_{Mg}	0·973	0·970	0·926	0·939	0·919	0·917	0·857	0·940	0·940	0·927

$X^*_{Mg} = Mg/(Fe^{2+} + Mg)$.
[1]35% of Fe^{tot} was assumed to be Fe^{3+}, based on average values of Fe^{3+} in sapphirine (after Grew *et al.*, 1999).

adjacent to garnet and sapphirine. Orthopyroxene X_{Mg} compositions typically decrease from core domains (0·89–0·91) to schistose rinds (0·84–0·87; Pod 10 $\approx$ 0·81). Sillimanite-rich gneiss and sapphirine–sillimanite gneiss orthopyroxenes have $X_{Mg} \approx 0{\cdot}84$–$0{\cdot}86$, which is similar to, or lower than the schistose rinds, with the exception of Pod 10 (Table 1). Individual orthopyroxene porphyroblasts show a consistent rimward decrease in Al_2O_3 from a broad core plateau that is high in Al_2O_3 (up to 9·5 wt %) to narrow (<35 μm), comparatively Al_2O_3-poor rims (>3 wt %; Fig. 6a). Zoning in Al_2O_3 is most marked when orthopyroxene is adjacent to cordierite or plagioclase, and in some cases significant rimward depletions in Al_2O_3 are observed in orthopyroxene adjacent to sapphirine (Fig. 6b) and phlogopite. Fe^{3+} has been calculated for orthopyroxene from charge balance based on four cations and six oxygens; contents are minor (0·030 $\pm$ 0·02 cations p.f.u.) and show no systematic

Table 2b: Representative electron microprobe analyses of minerals in typical quartz-absent metapelites

	Garnet				Cordierite			Plagioclase			Biotite		
Pod/zone:	10 (core A)	10 (core A)	10 (rind)	2 (rind)	1 (core)	10 (rind)		1 (sill−gn)	10 (sill−spn gn.)		1 (core)	1 (core)	10 (core B)
Sample:	OG588	OG588	OG581	OG567B	OG573	OG581		OG570	OG582A		OG522A	OG522A	OG587
Analysis:	1.14 Spr	2.2 Spr	1.3 adj Pl	2.13 in Spr	4.1 rim on Opx	1.62 adj Grt		1.1 Pl	3.3 adj Opx		9.3 adj. Opx	9·1	1A.1 core
wt %													
SiO_2	41·692	41·643	40·400	40·915	50·246	49·605		61·119	52·136		39·114	39·596	39·386
TiO_2	0·012	0·000	0·002	0·013	0·000	0·000		0·002	0·012		3·535	3·526	3·615
Al_2O_3	24·496	24·393	23·049	23·913	34·153	33·756		24·655	30·105		15·401	15·615	15·459
Cr_2O_3	0·038	0·004	0·079	0·034	0·000	0·000		0·013	0·001		0·063	0·106	0·075
FeO	9·080	9·781	19·034	16·424	0·828	1·749		0·018	0·349		5·017	5·026	4·389
MnO	0·166	0·093	0·480	0·416	0·027	0·009		0·000	0·041		0·022	0·042	0·005
MgO	21·277	22·610	15·764	19·019	13·405	12·668		0·000	0·419		21·908	22·192	22·266
CaO	2·916	1·524	1·325	0·850	0·041	0·035		6·161	12·495		0·001	0·000	0·000
Na_2O	0·024	0·024	0·019	0·058	0·062	0·026		8·407	4·251		0·294	0·266	0·266
K_2O	0·000	0·015	0·000	0·000	0·012	0·012		0·144	0·242		9·056	9·185	8·693
F											1·575	1·282	1·189
−O equiv. F											0·663	0·540	0·501
Total	99·701	100·087	100·152	101·646	98·774	97·860		100·519	100·051		95·323	96·296	94·842
No. ox	12	12	12	12	18	18		8	8		22	22	22
Cations p.f.u.													
Si	2·954	2·939	2·976	2·930	4·978	4·979		2·706	2·368		5·506	5·524	5·548
Ti	0·001	0·000	0·000	0·001	0·000	0·000		0·000	0·000		0·374	0·370	0·383
Al	2·046	2·029	2·002	2·019	3·989	3·995		1·287	1·612		2·556	2·568	2·567
Cr	0·002	0·000	0·005	0·002	0·000	0·000		0·000	0·000		0·007	0·012	0·008
Fe^{tot}	0·538	0·577	1·173	0·984	0·069	0·147		0·001	0·013		0·591	0·586	0·517
Mn	0·010	0·006	0·030	0·025	0·002	0·001		0·000	0·002		0·003	0·005	0·001
Mg	2·247	2·378	1·731	2·030	1·979	1·895		0·000	0·028		4·596	4·614	4·674
Ca	0·221	0·115	0·105	0·065	0·004	0·004		0·292	0·608		0·000	0·000	0·000
Na	0·003	0·003	0·003	0·008	0·012	0·005		0·722	0·374		0·040	0·036	0·036
K	0·000	0·001	0·000	0·000	0·002	0·002		0·008	0·014		0·813	0·817	0·781
F									0·701		0·566	0·530	
Total	8·023	8·049	8·022	8·063	11·034	11·027		5·016	5·020		15·188	15·099	15·046
X_{Mg}	0·81	0·80	0·60	0·67	0·97	0·93	X_{An}	0·29	0·61	X_{Mg}	0·89	0·89	0·90
X_{Alm}	0·18	0·19	0·39	0·32			X_{Ab}	0·71	0·38				
X_{Grs}	0·07	0·04	0·03	0·02									
X_{Pyp}	0·74	0·77	0·57	0·65									
X_{Sps}	0·00	0·00	0·01	0·01									

variation or zoning features. Fe^{3+} in Fe^{total} averages 0·11 ± 0·08, increasing X_{Mg} by generally less than 0·03 units, but is higher in some cases (Tables 1 and 2a).

Biotite

All biotite is close to phlogopite in composition [classified after Deer *et al.* (1992, p. 284)]. Consistent with other ferromagnesian minerals, X_{Mg} of phlogopite decreases systematically from core zones (0·93–0·90) to schistose rinds (0·85–0·88), whereas phlogopites from sillimanite-rich and sapphirine–sillimanite gneiss are similar in composition or slightly less magnesian ($X_{Mg} \approx$ 0·85–0·89). Total F in phlogopite is commonly between 1·2 and 1·5 wt %, with no systematic variation between zones or pods. As F rarely accounts for more than 2% of the

Table 3: SIMS analyses of selected kornerupine grains from sample OG566 (Pod 2)

	krn1	krn3	krn4	krn5	krn6	krn7	krn8	krn9	Average
ppm									
Si	137890	137700	137700	137700	137700	137700	137700	137700	
Mg	92436	92684	93505	92584	92419	93191	93300	93079	92900
Fe	27874	28599	28817	28879	28482	28743	29300	29252	28743
Mn	441	444	436	454	467	457	445	438	448
Ti	681	680	656	743	523	626	771	771	681
Cr	366	403	436	401	339	360	429	457	399
Ca	217	222	217	217	206	209	210	211	214
Na	359	364	353	357	336	330	386	374	357
K	3·5	3·4	3·5	3·7	4·1	3·7	3·7	3·65	3·66
Li	148	152	159	152	165	162	146	145	154
Be	87·8	82·9	90·1	94·2	89·9	91·3	95·6	92·8	90·6
B	3068	3061	3004	2805	2989	2957	2822	2811	2940
P	321	329	338	391	399	328	411	347	358
Cl	315	323	311	299	310	319	318	318	314
F	4753	5021	4797	4697	4777	4803	4742	4696	4786
Sc	27·7	27·8	25·6	25·5	29·2	28·1	24·5	24·5	26·6
V	136	136	139	141	131	136	140	144	138
Co	18	18	19	18	19	19	19	20	19
Ga	49	53	53	52	50	50	56	57	53
Y	4·98	5·31	5·15	4·72	4·92	5·04	5·19	4·87	5·02
Zr	3·03	2·73	2·68	3·05	1·75	2·78	3·17	3·5	2·84
Nb	0·15	0·095	0·113	0·155	0·118	0·175	0·213	0·087	0·14
wt %									
H_2O	0·802	0·841	0·871	0·804	0·845	0·864	0·879	0·853	0·845
Major components recalculated to wt % oxide									
wt %									
SiO_2	29·58	29·54	29·54	29·54	29·54	29·54	29·54	29·54	29·54
MgO	17·51	17·56	17·72	17·54	17·51	17·66	17·68	17·64	17·60
FeO	3·584	3·677	3·705	3·713	3·662	3·696	3·767	3·761	3·70
MnO	0·057	0·057	0·056	0·059	0·060	0·059	0·057	0·057	0·06
TiO_2	0·114	0·113	0·109	0·124	0·087	0·104	0·129	0·129	0·11
Cr_2O_3	0·053	0·059	0·064	0·059	0·050	0·053	0·063	0·067	0·06
Na_2O	0·048	0·049	0·048	0·048	0·045	0·044	0·052	0·050	0·05
B_2O_3	0·976	0·974	0·956	0·893	0·951	0·941	0·898	0·894	0·94
H_2O	0·802	0·841	0·871	0·804	0·845	0·864	0·879	0·853	0·84
						Total wt % oxides (SIMS)			53·33
						Al_2O_3 (EMP)			47·4
						Total			100·73
X_{Mg}	0·898	0·896	0·896	0·895	0·896	0·896	0·894	0·894	0·895

Using modified relative ion yield for Mg based on feldspar (high Al/Si); total wt % oxide value based on recalculated wt % oxides for the major elements, with Al_2O_3 taken from average electron microprobe analyses of kornerupine.

total percentage of elements in the phase, up to 6 wt % of total oxides is unaccounted for in the analysis. This is inferred to be H_2O or Cl in the hydroxyl site, suggestive of a relatively hydrous phlogopite.

Garnet

General grain compositions are variable within and between pods, although predominantly following the Mg zoning patterns already described for other minerals.

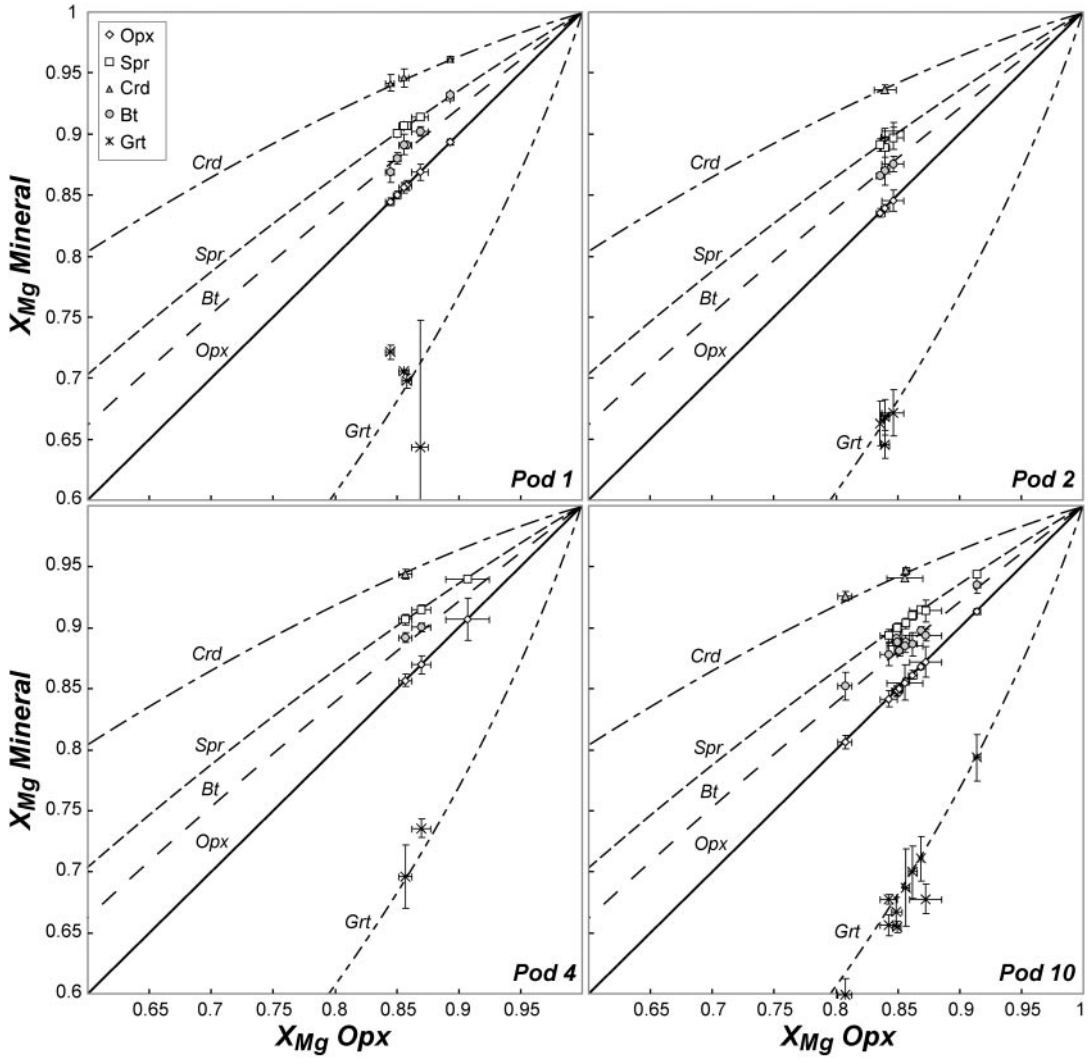

Fig. 5. Mineral X_{Mg} distribution diagram for Pods 1, 2, 4 and 10. Average mineral X_{Mg} compositions are plotted against the average orthopyroxene X_{Mg} particular to the sample. The consistent relationship between mineral X_{Mg} and orthopyroxene X_{Mg} across each of the four pods illustrated should be noted. Dashed curves are Mg distribution lines that describe the X_{Mg} of mineral x for a given orthopyroxene X_{Mg}. Error bars indicate the standard deviation of average values at 1σ level.

The most magnesian garnet occurs as inclusions in sapphirine in the core zone of Pod 10 [$X_{Pyp} = 0{\cdot}74$–$0{\cdot}77$, where $X_{Pyp} = Mg/(Mg + Fe^{tot} + Ca + Mn)$] and Pod 1 ($X_{Pyp} = 0{\cdot}67$–$0{\cdot}70$). In general, X_{Grs} [$Ca/(Mg + Fe^{tot} + Ca + Mn)$] = 0·02–0·03. Most garnets display a systematic decrease in X_{Pyp} between the core and schistose rind (Table 1), with minor increases in X_{Grs} and X_{Alm} [$Fe^{tot}/(Mg + Fe^{tot} + Ca + Mn)$]. Sillimanite-rich and sillimanite–sapphirine gneiss typically have garnet compositions similar to, or slightly more magnesian than schistose rind garnet. Garnet porphyroblasts, which are preserved only in Pods 2 and 10, commonly preserve a rimward decrease in X_{Pyp}, with a broad core compositional plateau and narrow zoned rim (e.g. Fig. 7b). The core composition of some garnet grains in the schistose rinds may be as high as $X_{Pyp} = 0{\cdot}67$ (Pod 2), similar to the composition of garnet inclusions in sapphirine from core domains. The composition of the rims of these grains is equivalent to that of smaller garnet porphyroblasts and inclusions in sapphirine in the schistose rind domains.

Kornerupine

Electron microprobe analyses indicate $X_{Mg} \approx 0{\cdot}89$–$0{\cdot}91$ (where $Fe^{2+} = Fe^{tot}$) and a $(Mg,Fe)O{:}Al_2O_3{:}SiO_2$ ratio that is close to 11:10:11, such that kornerupine lies to the Si-poor side of the Crn–Opx tie-line in MAS (Fig. 7c). However, considering the Fe^{3+} content in Fe^{total} [after Grew *et al.* (1999): Fe^{3+} in kornerupine is inferred to be equal to that estimated for associated sapphirine],

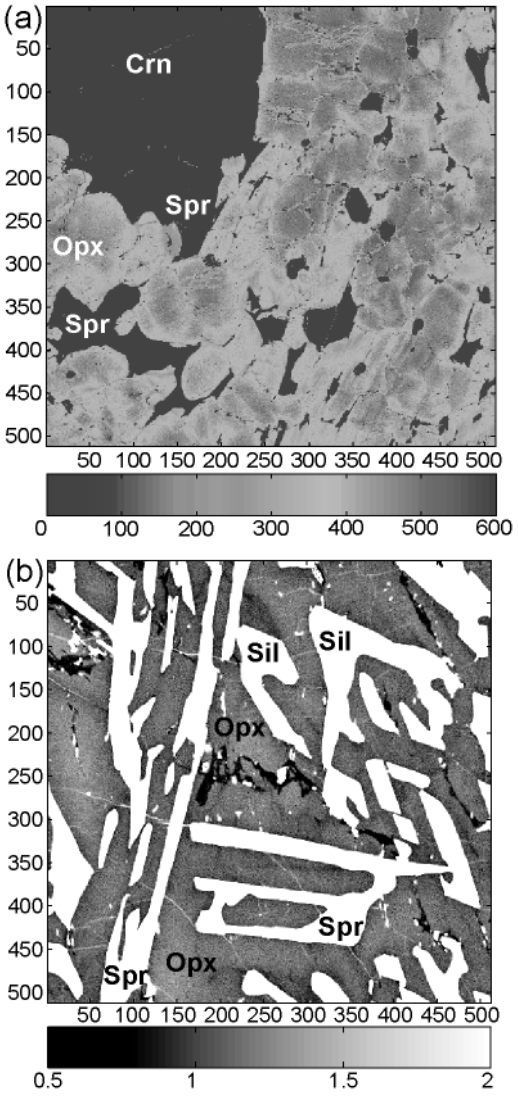

Fig. 6. Grey-scale X-ray intensity maps (512 × 512 pixels) for selected textures illustrating Al zoning in orthopyroxene. (a) Pod 1 edge of core (sample OG524—same map area as Fig. 2a; map is for raw count intensity only). Dark cores in the orthopyroxene correspond to high Al values, zoning to light, lower Al rims. Some zoning departs from rim-parallel patterns with Al depletion along planar zones that are oblique to the grain margin, interpreted to reflect enhanced diffusion along cleavage planes (e.g. Harley, 1998*b*; Harley & Motoyoshi, 2000). (b) Pod 4 sillimanite-rich gneiss (sample OG577—same map area as Fig. 2e). Al (raw count intensity recalculated to cations per 24 oxygens) is high in the cores, decreasing toward rims.

approximately 35% in the Oygarden samples, increases X_{Mg} to ≈0·93–0·94. These values are similar to X_{Mg} values previously recorded for kornerupine (Droop, 1989; Goscombe, 1992; Vry, 1994; Carson *et al.*, 1995; Friend, 1995; Grew, 1996). In addition to a change in X_{Mg}, removing Fe^{3+} from Fe^{total} shifts the position of kornerupine to being effectively collinear with orthopyroxene–corundum in MAS. Total Al cations p.f.u. (for 21·5 oxygens) are approximately 6·9 and Al^{IV} [=5 – (Si + B)] is calculated to lie between 1·06 and 1·16. The Oygarden kornerupines are 'boron-poor' examples (after Friend, 1995), with nine SIMS analyses yielding an average of 0·94 wt % B_2O_3, 0·48 wt % F, 0·85 wt % H_2O, 0·05 wt % Na_2O, 91 ppm Be and 314 ppm Cl (see Table 3 for full analyses).

Other phases

In cordierite (where present), X_{Mg} varies from cores (0·96–0·97) to schistose rinds (0·94–0·95), consistent with the X_{Mg} trends recorded by the other minerals (Table 1). Cordierite in sillimanite-rich gneiss commonly has a similar composition to that in the schistose rind (X_{Mg} = 0·94–0·95). Plagioclase occurs in a number of zones in Pod 10, and only in sillimanite-rich gneiss in Pod 1, and has a variable composition with X_{An} [=Ca/[Ca + Na + K)] between 0·30 and 0·55. Calcium contents are higher in samples from Pod 10 (average X_{An} ≈ 0·50) and individual grains commonly preserve a rimward increase in X_{An}. Zoning is especially pronounced where plagioclase is adjacent to garnet. Sillimanite is near pure Al_2SiO_5, with Fe being the only impurity (<0·3 wt % Fe_2O_3, measured as FeO). Fe values show no systematic variation when in association with sapphirine. Corundum contains less than 0·15 wt % Fe_2O_3 and less than 0·3 wt % Cr_2O_3.

MINERAL CHEMISTRY OF QUARTZ-PRESENT METAPELITE

Garnet from quartz-bearing metapelitic gneiss is a pyrope–almandine mix (X_{Alm} = 0·35–0·46, and X_{Pyp} = 0·51–0·62) with low grossular contents (X_{Grs} = 0·02–0·03). Large garnet grains (>2 mm in diameter) show a subtle rimward increase in Fe and a decrease in Mg content, commonly by approximately X_{Alm} = 0·03. Orthopyroxene has X_{Mg} = 0·75–0·83 [Mg/(Mg + Fe^{tot})] with alumina contents varying between 0·37 and 0·11 cations per six oxygens, and shows a consistent rimward decrease in porphyroblastic orthopyroxene of up to 0·17 cations. X_{Mg} of cordierite ranges between 0·90 and 0·94 and rarely preserves zoning. However, some symplectic cordierite has higher Mg contents than grains adjacent to biotite or garnet. Plagioclase is oligoclase in composition, with X_{An} = 0·18–0·32 and X_{Ab} = 0·80–0·66. Where plagioclase occurs as exsolution lamellae in perthite, it has the same composition as larger matrix grains. Alkali feldspar is sanidine to orthoclase in composition, with X_{Or} = 0·73–0·92 and X_{Ab} = 0·27–0·08. Rare analyses taken from exsolution lamellae in K-feldspar have higher albite components (X_{Ab} ≤ 0·87). Biotite compositions range from phlogopite to eastonite, with

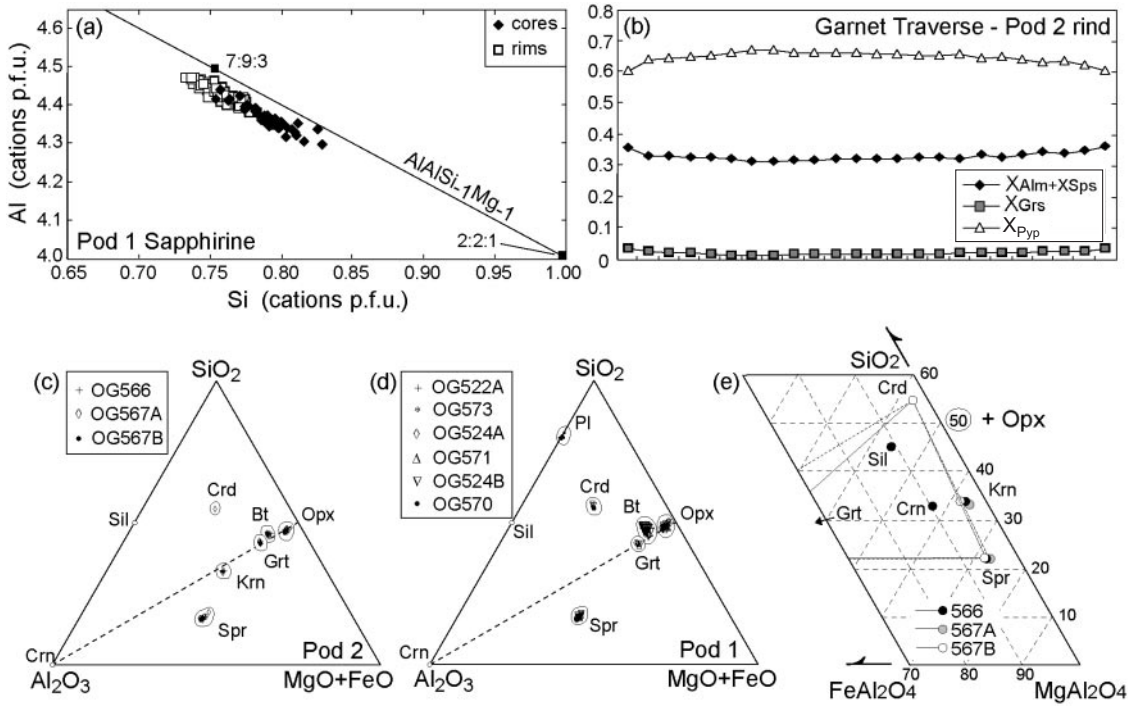

Fig. 7. (a) Al:Si zoning in sapphirine, showing high-Al rims (□) vs higher-Si cores (◆). (b) Compositional traverse across a garnet porphyroblast from the rind of Pod 2. Garnets typically show a decrease in X_{Pyp} mirrored by an increase in X_{Grs} and $X_{Alm} + X_{Sps}$ adjacent to rims. The garnet is approximately 0·5 mm in diameter. (c) (MgO + FeO)–SiO_2–Al_2O_3 ternary plot for Pod 2 (Krn-bearing); it should be noted that kornerupine in this plot is uncorrected for Fe^{3+} in total Fe, and therefore plots just below the Opx–Crn tie-line. (d) (MgO + FeO)–SiO_2–Al_2O_3 ternary plot showing chemographic relationships between phases from Pod 1 (Krn-absent). (e) Partial ternary diagram illustrating the position of the minerals Crd, Sil, Crn, Krn, Spr and Grt projected from Opx onto the SiO_2–$FeAl_2O_4$–$MgAl_2O_4$ (quartz–hercynite–spinel) plane, using mineral compositions corrected for Fe^{3+}. The minor deviation of Krn to the magnesian side of the Opx–Spr–Crd plane should be noted.

X_{Mg} of between 0·79 and 0·91. Sillimanite generally has less than 0·5 wt % Fe_2O_3 (analysed as FeO).

BULK-ROCK GEOCHEMISTRY

Bulk-rock composition data were obtained using standard X-ray fluorescence (XRF) techniques at the University of New South Wales and are available in Supplementary Data Table 1, which may be downloaded from the *Journal of Petrology* website at http://www.petrology.oupjournals.org/. The components MgO–FeO–SiO_2–Al_2O_3 make up 97–98% of core samples and 94–97% of schistose rind samples, with the remainder being mostly K_2O. Compositional relationships are therefore easily compared with analysed mineral compositions using a MAS ternary diagram (Fig. 8). The whole-rock analyses confirm that the rocks are undersaturated with respect to silica (38–47%), are highly magnesian (X_{Mg} = 0·85–0·93), and have core compositions characteristically low in CaO and Na_2O. Data indicate systematic K enrichment in the transition zones and schistose rinds of the pods, an increase that is reflected in the increased modal abundance of phlogopite. In addition, most pods also show a minor, although systematic, enrichment in Fe and Si in the rinds. No major elements exhibit consistent depletion patterns; however, an apparent decrease in Mg was observed in data from some pods. Ti is commonly depleted in transition zones and enriched in the schistose rind correlating with a decrease in rutile abundance and grain size with increasing distance from the core. This may also indicate mobility of Ti from the core into the schistose rind where it has been incorporated in phlogopite. The presence of plagioclase with a significant albite component ($X_{Ab} = 0·7$ in Pod 1 outer zones; $X_{Ab} = 0·45$–0·69 in Pod 10; Table 1) suggests that a proportion of Na was present. There are no consistent zoning patterns with respect to Na, although some pods do have a rimward increase (Pods 1 and 10), therefore Na metasomatism accompanying silica cannot be confirmed.

On a MAS compatibility diagram, most bulk-rock compositions plot within the orthopyroxene–sillimanite–sapphirine tie-triangle and commonly on the silica-poor side of the orthopyroxene–corundum tie-line (Fig. 8). The compositions plot between garnet and phlogopite, and close to orthopyroxene, which correlates with the high proportion of orthopyroxene within core assemblages and abundance of phlogopite in rind assemblages.

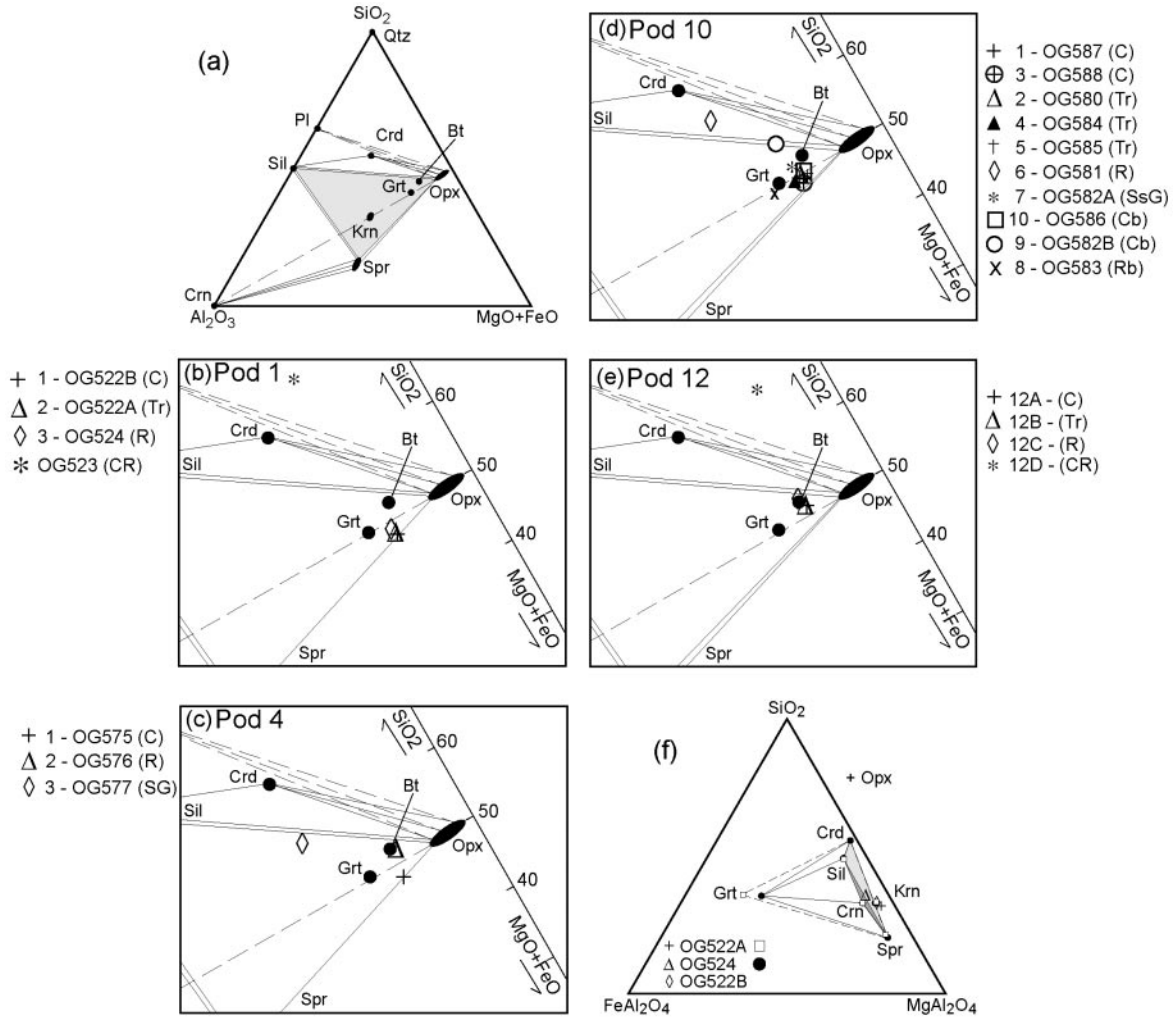

Fig. 8. (a) (MgO + FeO)–Al_2O_3–SiO_2 ternary diagram showing the positions of analysed minerals. This diagram does not consider Fe–Mg relations between phases. (b)–(e) enlarged portions of (a), showing the positions of bulk compositions as determined by XRF for Pods 1, 4, 10, and 12. Abbreviations to the right of each sample number: C, core zone; Cb, core zone from Pod 10B; Tr, transition zone; R, schistose rind; Rb, schistose rind from Pod 10B; CR, country rock; SG, sillimanite-rich gneiss; SsG, sillimanite–sapphirine gneiss. (f) FMAS compatibility diagram for Pod 1, showing phase (symbol to the right of sample number) and selected bulk-rock compositions (symbol to the left of sample number) projected from orthopyroxene. Each bulk composition and mineral has been projected from the orthopyroxene composition particular to that sample.

Exceptions to this include the quartz-bearing country rock from Pods 1 and 12, and samples OG577 (Pod 4) and OG581 (Pod 10). Sample OG577 is from sillimanite-rich gneiss that envelopes Pod 4 and its composition plots close to the orthopyroxene–sillimanite tie-line. Sample OG581 (schistose rind) plots above the orthopyroxene–sillimanite tie-line within the stability field orthopyroxene–sillimanite–cordierite, which corresponds to the observed textures and the absence of sapphirine in the assemblage.

THERMOBAROMETRY

The majority of quartz-absent assemblages described here are not appropriate for conventional thermobarometry. As a result, P–T estimates were made from garnet–orthopyroxene-bearing S_3 and S_4 assemblages from quartz-bearing metapelite that formed layers within the same outcrop as the silica-undersaturated metapelite. Average P and T calculations using the coarse-grained assemblage garnet, orthopyroxene, plagioclase, sillimanite, biotite, quartz and cordierite (sample OG562) using THERMOCALC v.3.0 [Powell & Holland (1988), based on the internally consistent dataset of Holland & Powell (1998)], gave an average $P = 9{\cdot}9 \pm 0{\cdot}3$ kbar (for $T = 850°C$; $a_{H_2O} = 1{\cdot}0$; 1σ) and an average $T = 844 \pm 27°C$ (for $P = 10$ kbar; 1σ). Using $a_{H_2O} = 0{\cdot}5$ reduced pressures by 1 kbar but raised temperatures by 50–60°C, whereas using $a_{H_2O} = 0{\cdot}1$ reduced pressures by only 0·5 kbar and raised temperatures by ≈140°C.

Using the 'average P–T' function on the same assemblage gave $P = 10{\cdot}1 \pm 0{\cdot}6$ kbar and $T = 875 \pm 65°C$ (1σ). Excluding cordierite from this assemblage gave slightly lower pressure and similar temperature estimates: average P–T of $P = 8{\cdot}7 \pm 1{\cdot}3$ kbar and $T = 876 \pm 66°C$ (1σ). A second sample (OG589) gave similar, although poorly constrained, results for the S_4 assemblage garnet, orthopyroxene, plagioclase, biotite, cordierite and quartz, with an average P–T estimate of $P = 8{\cdot}4 \pm 2{\cdot}1$ kbar and $T = 819 \pm 156°C$ (1σ).

Temperature estimates for suitable quartz-absent samples where garnet and orthopyroxene are in textural contact and interpreted to be in chemical equilibrium, or inferred to have originally been in textural contact, have also been obtained using garnet–orthopyroxene equilibria (Fe–Mg: Ganguly *et al.*, 1996; Mg–Al: Harley & Green, 1982; Fe–Al: Aranovitz & Berman, 1997). A 10 kbar pressure estimate, obtained above, was used. Adjacent rim compositions of garnet and orthopyroxene produced estimates of $T \approx 810$–$910°C$ (for $P = 10$ kbar; Fe–Mg calibration) and $T \approx 850$–$960°C$ (for $P = 10$ kbar; Mg–Al calibration). The Fe–Al calibration was consistently lower than the Fe–Mg and Mg–Al calibrations and gave estimates of $T \approx 740$–$845°C$ (for $P = 10$ kbar). To investigate the effects of post-peak re-equilibration of Fe–Mg between orthopyroxene and garnet, the approach of Fitzsimons & Harley (1994) was used to 'back-calculate' the peak composition of garnet–orthopyroxene pairs. This technique produced internally consistent (convergent) estimates generally in the range $T \approx 910$–$960°C$. Results obtained using garnet–orthopyroxene thermobarometers alone are only indicative of the general metamorphic conditions, and do not provide tight constraints on the P–T evolution. However, these results are consistent with estimates from THERMOCALC and those obtained using conventional garnet–orthopyroxene–plagioclase–quartz thermobarometry (see Supplementary Data Tables 2 and 3, which may be downloaded from the *Journal of Petrology* website). In all, the application of thermobarometry suggests peak or near-peak P–T conditions of $P \approx 9$–10 kbar and $T \approx 850$–$950°C$.

REACTION HISTORY AND PHASE RELATIONS

Reaction textures observed in the orthopyroxene–sapphirine granulites occur in all compositional zones. This implies that the reaction textures post-date the development of the compositional zones and hence were not a direct result of interaction with a metasomatic fluid. Instead, the textures are interpreted to have been formed as a consequence of changes in ambient pressure–temperature conditions. For the purposes of describing the phase relations, the minerals orthopyroxene–corundum–sapphirine–sillimanite–cordierite–garnet–spinel have been investigated in the simplified FeO–MgO–Al_2O_3–SiO_2 system (FMAS). By comparing the assemblages and reaction textures observed with existing petrogenetic grids (Waters, 1986; Hensen, 1987), a qualitative partial P–T grid involving FMAS univariant reactions has been constructed (Fig. 9), and relevant FMAS divariant equilibria within this system have been modelled in terms of their MAS end-member analogues. The new grid observes known ΔV_r contraints and restricts sapphirine-bearing assemblages to high temperatures by its terminal reaction relations. In addition, the grid restricts orthopyroxene–corundum to low temperatures relative to sapphirine, cordierite to low pressures and garnet to high pressures. The new reaction grid differs from previously published grids (e.g. Windley *et al.*, 1984; Droop, 1989; Goscombe, 1992) in ignoring gedrite and spinel, and in being focused on the high-pressure reactions involving assemblages including orthopyroxene and corundum. In contrast to the grids of Droop (1989) and Goscombe (1992), the grid presents FMAS univariant reactions linked to MAS terminations and divariant equilibria. The new grid incorporates and satisfies the topology of the [Krn Spl Qtz] univariant reaction (Hensen & Green, 1973; Hensen, 1986, 1987) and the kornerupine-present experimental results of Wegge & Schreyer (1994), and is consistent with observations made for similar rocks from the Limpopo Belt (Windley *et al.*, 1984; Droop, 1989).

Kornerupine-absent equilibria

Early Opx–Crn and pre- to syn-S_3 assemblages

The S_3 minerals sapphirine, orthopyroxene and sillimanite each contain relics of Mg-Grt. Although from the textures it is difficult to uniquely deduce reactions leading to the early formation of this garnet, its decrease in modal abundance suggests the traversal of the divariant FMAS [Crn Spl Crd] reaction

$$\mathrm{Grt} = \mathrm{Spr} + \mathrm{Opx} + \mathrm{Sil} \qquad (1a)$$

with decreasing pressure and rising or falling temperature. This is, therefore, suggestive of a clockwise P–T path, although the precise dP/dT of this path segment cannot be constrained. In some instances corundum is produced at the apparent expense of garnet, leading to the [Spl, Crd, Sil] assemblage orthopyroxene, sapphirine and corundum, with minor garnet. This can be explained by the end-member MAS analogue

$$\mathrm{Grt} = \mathrm{Opx} + \mathrm{Crn}. \qquad (1b)$$

Orthopyroxene and corundum can also be produced from sapphirine and cordierite on an up-pressure path in highly magnesian bulk compositions. However, there is no textural or mineralogical evidence for an early

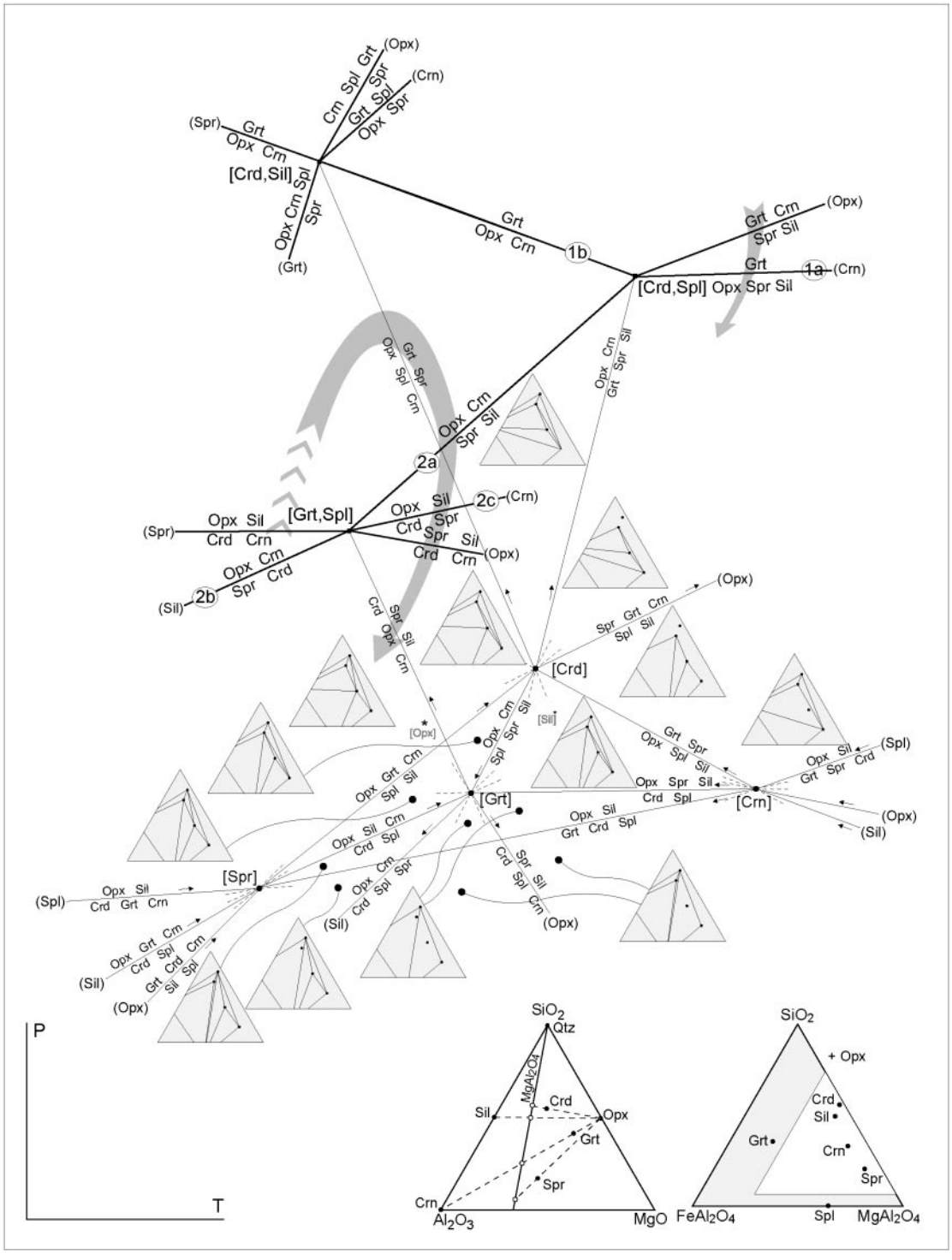

Fig. 9. Qualitative *P–T* grid for the silica-undersaturated portion of the FMAS system, based on the grid of Hensen (1987). Thin lines are univariant reactions in the FMAS system (taken from Hensen, 1987), and thicker lines are FMAS divariant reactions modelled as MAS analogues that emanate from MAS invariant points. The estimated slopes of FMAS divariants 1a, 1b, 2a, 2b, and 2c are after Ouzegane *et al.* (2003), using the thermodynamic dataset of Holland & Powell (1998). The slope of the [Grt Spl Spr] FMAS divariant is after Hensen (1987) and is based on Newton (1972). Arrows on the FMAS reaction lines indicate increasing X_{Mg} of phases. FMAS compatibility diagrams for each field in the FMAS grid show phase relations projected from orthopyroxene onto the SiO_2–$FeAl_2O_4$–$MgAl_2O_4$ plane. Circled numbers on MAS univariant curves refer to reaction numbers discussed in the text. The abbreviations [Opx] and [Sil] given in grey text refer to the location of the Opx- and Sil-absent metastable FMAS invariant points.

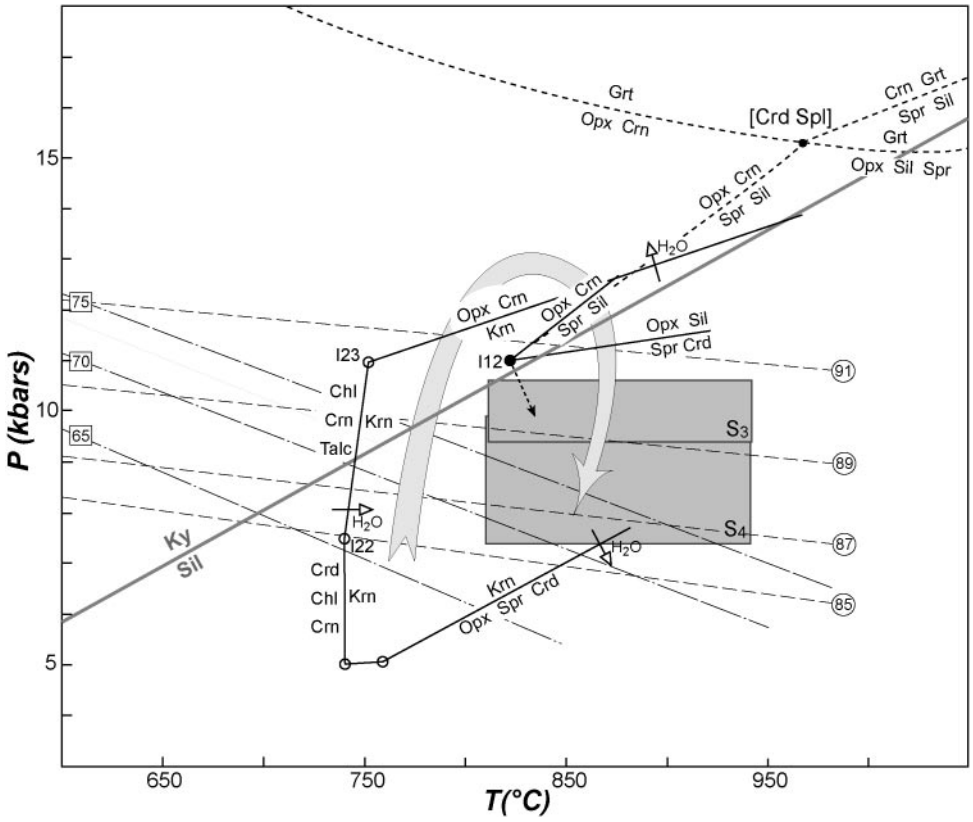

Fig. 10. *P–T* path drawn relative to the calculated or experimentally located positions in *P–T* space of equilibria pertinent to the Oygarden samples. The end-member (MAS) reactions around the [Crd Spl] invariant point are indicated by the thick, short-dashed lines [positions after Ouzegane *et al.* (2003), calculated from the Holland & Powell (1998) internally consistent thermodynamic dataset]. X_{Mg} isopleths for garnet (dot–dashed lines, values $X_{Pyp} \times 100$) and orthopyroxene (dashed lines, values $X_{Mg} \times 100$) are for coexisting garnet and orthopyroxene in relation to the MAS reaction Grt = Opx + Crn. The position of the Ky–Sil phase boundary was determined using THERMOCALC v.3.1 (dataset created 19 September 1999). The location of the [Grt Spl] absent MAS invariant (I12) is based on the experimental data of Ackermand (1970) and MAS grid of Ouzegane *et al.* (2003). This same invariant point was indirectly constrained by Schreyer & Seifert (1969) to occur at $P < 10$ kbar. The dashed arrow emanating from this invariant point indicates the direction in which this point will move with decreasing X_{Mg}. The I22 and I23 invariant points and slopes of reactions emanating from these points in the boron-free Krn-bearing system are taken from Wegge & Schreyer (1994). Arrows denoted 'H_2O' indicate the direction in which the kornerupine-present reactions will shift with increasing water activity. The shaded areas indicate average *P–T* estimates for S_3 and S_4 garnet–orthopyroxene assemblages discussed in the text.

sapphirine + cordierite assemblage, or sapphirine + cordierite + orthopyroxene in garnet-absent cases.

Reaction (1b) lies at high pressure in Fig. 9 and has a slope that is constrained using the thermodynamic dataset of Holland & Powell (1998), and is consistent with the same reaction as calculated by Ouzegane *et al.* (2003). This Mg end-member reaction lies at $P = 16{\cdot}25 \pm 0{\cdot}25$ kbar (1σ) for $T = 850°C$ and $X_{MgTs} = 0{\cdot}12$ (Fig. 10; Gasparik & Newton, 1984). However, the reaction is displaced to lower pressures with increasing Fe content in garnet. For example, using the highest recorded magnesium content for relic garnet from a core zone ($X_{Pyp} = 0{\cdot}77$), with the corresponding orthopyroxene for that zone ($X_{Mg} = 0{\cdot}88$), displaces this curve to $P \approx 11{\cdot}7$ kbar for $T = 850°C$ (calculated using THERMOCALC, v.3.1, Powell & Holland, 1988). This pressure may be considered an upper limit to conditions reached during D_3, and agrees with textural evidence for the absence of kyanite either as inclusions in garnet or pseudomorphed by sillimanite. The position of the kyanite–sillimanite boundary between 800 and 850°C is $P = 10{\cdot}2$–$11{\cdot}3 \pm 0{\cdot}11$ kbar (1σ, Fig. 10; calculated using THERMOCALC, v.3.1, Powell & Holland, 1988). These pressure estimates are also consistent with estimates made using S_3 assemblages from mafic granulite ($P \approx$ 9–10 kbar; Kelly *et al.*, 2000) and quartz-bearing metapelitic gneiss described above.

Post-S_3/S_4 reaction textures—corundum breakdown

Reaction textures that are preserved in most pods are random in habit. They overgrow S_3 in core and transition zones, and S_4 in schistose rinds, and therefore formed late- to post-D_4. The dominant reaction texture observed

in corundum-bearing samples involves single- or double-layer coronas of sapphirine and sillimanite separating corundum from orthopyroxene. These textures may be explained by the MAS model reaction

$$2\mathrm{Opx} + 3\,\mathrm{Crn} = \mathrm{Spr} + \mathrm{Sil} \qquad (2a)$$

(Fig. 9), which can be crossed with decreasing pressure and/or rising temperature. This reaction drives orthopyroxene to lower X_{Mg} but, most significantly, reacts out corundum. The slope of reaction (2a) is uncertain. Hensen (1987), based on the experimental data of Ackermand (1970), proposed a steeply positive slope ($\mathrm{d}P/\mathrm{d}T \geq 50\,\mathrm{bar}/^{\circ}\mathrm{C}$), whereas others have suggested moderate, positive slopes (Bertrand *et al.*, 1992: $\mathrm{d}P/\mathrm{d}T =$ 10–20 bar/°C), or steep negative slopes (Kihle & Bucher-Nurminen, 1992: $\mathrm{d}P/\mathrm{d}T = -50$ to $-70\,\mathrm{bar}/^{\circ}\mathrm{C}$, based on the thermodynamic data of Berman *et al.*, 1985). A moderately steep, positive slope consistent with Ouzegane *et al.* (2003; $\mathrm{d}P/\mathrm{d}T \approx 25\,\mathrm{bar}/^{\circ}\mathrm{C}$) has been used here to allow this reaction to link FMAS divariant equilibria generated from adjacent FMAS univariant reactions (Fig. 9).

In zones with higher $X_{\mathrm{SiO_2}}$ (outer transition zone and schistose rinds), cordierite becomes increasingly abundant and appears as a replacement phase. Rather than by direct replacement of corundum (+ orthopyroxene), the cordierite selectively replaces those textural domains in which sapphirine, with or without sillimanite, already appears to have formed. That is, the development of sapphirine and cordierite symplectites separating orthopyroxene and corundum (Fig. 3c) was not a situation of crossing reaction (2b) (Fig. 9), which would imply initial MAS tie-triangles sapphirine–orthopyroxene–corundum and orthopyroxene–corundum–cordierite. In addition, crossing this reaction is inconsistent with the formation of orthopyroxene and sillimanite in lower $X_{\mathrm{SiO_2}}$ bulk compositions. As an alternative, we suggest that, following reaction (2a), the MAS analogue

$$4\mathrm{Opx} + 8\,\mathrm{Sil} = \mathrm{Spr} + 3\,\mathrm{Crd} \qquad (2c)$$

was crossed. Reactions (2a) and (2c) emanate from the same invariant point and may be crossed consecutively with decreasing pressure, at rising or constant temperature and $X_{\mathrm{SiO_2}}$ (Fig. 11a). Volume data for the phases predict that considerably more cordierite than sapphirine will be produced, which explains the extensive development of cordierite in the rind regions. In Fig. 9, reaction (2c) has been given a shallow, positive slope that agrees with a number of published grids (Hensen, 1987; Kihle & Bucher-Nurminen, 1992; Ouzegane *et al.*, 2003). Reactions (2a) and (2c) intersect at an MAS [Grt Spl] invariant point (Fig. 9), which has been constrained indirectly, using experiments on reactions (2a) and (2c), to lie at $P = 11 \pm 1{\cdot}5$ kbar and $T = 820 \pm 50^{\circ}\mathrm{C}$ (Fig. 10; Ackermand, 1970). With increasing Fe in the system, this MAS invariant point will be displaced as an FMAS univariant to lower pressures and higher temperatures, and will define the FMAS univariant reaction [Grt, Spl] (Figs 9 and 10).

Post-S_3/S_4 reaction textures—garnet breakdown textures

Where garnet occurs as medium- to coarse-grained porphyroblasts it is commonly surrounded by symplectites that are interpreted to have developed during or after D_4. Typically, garnet is surrounded and embayed by intergrowths involving orthopyroxene and sapphirine, with plagioclase and/or cordierite. These symplectites may be 'spinifex-like' in cross-section (e.g. OG582A; Fig. 3f) or comprise more coarse-grained intergrowths of elongate sapphirine with orthopyroxene (OG580). Small, relic garnet grains commonly occur within the symplectites, and may occur as inclusions within sapphirine. These textures are consistent with breakdown of garnet by the simultaneous progression from left to right, with decreasing pressure, of two component reactions in the CMAS and FMAS sub-systems:

$$\mathrm{CMAS}: 10\mathrm{Grt}_{(\mathrm{Pyr}_{33}\mathrm{Grs}_{67})} = 11\mathrm{Opx} + 2\mathrm{Spr} + 2\mathrm{An} \qquad (3a)$$

$$\mathrm{FMAS}: 8\mathrm{Grt} = 8\mathrm{Opx} + 3\mathrm{Spr} + \mathrm{Crd}. \qquad (3b)$$

The extent to which each of these reactions will occur is dependent on the initial X_{Pyp} and X_{Grs} content of the reacting garnet, with plagioclase and cordierite effectively interchangeable in terms of their Al:Si ratios and reaction roles. The predominance of plagioclase over cordierite as an inferred product from the breakdown of garnet in samples OG582 and OG580 suggests that the initial garnet had an appreciable X_{Grs} content. The preferential location of plagioclase adjacent to garnet has previously been interpreted to result from slow Ca diffusion relative to Fe–Mg (e.g. Spear, 1993). However, plagioclase is widespread in some Oygarden samples and found intergrown throughout the sapphirine and orthopyroxene symplectites. Remnant garnet grains also occur in many of these zones, suggesting that garnet was present as relatively large grains and in appreciable abundances (possibly >30%) in the peak metamorphic assemblage, prior to garnet breakdown. A further, localized garnet breakdown texture occurs in OG577. Here, cuneiform intergrowths of sapphirine and sillimanite with orthopyroxene (Fig. 3e) occur around large garnet grains, and sapphirine and sillimanite contain inclusions of garnet. These textures are interpreted to reflect the effects of decompression across a reaction similar to reaction (1a).

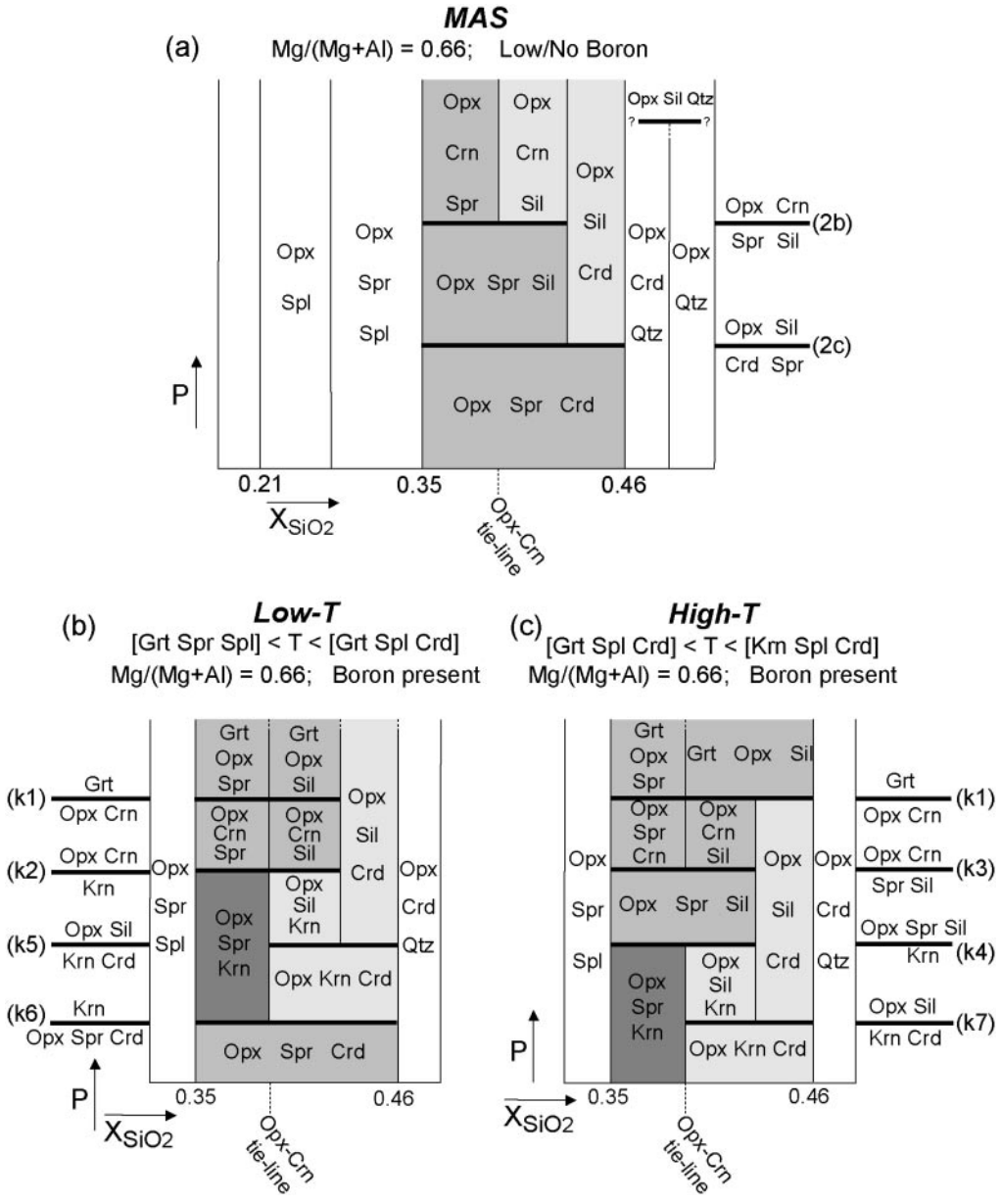

Fig. 11. Semi-quantitative P–X_{SiO_2} diagrams for the MAS univariants in Krn-absent and Krn-present systems. Vertical boundaries have been kept straight for simplicity. However, one expects that these field boundaries, with the exception of those between Crn-bearing assemblages, should deviate from straight lines with changing alumina content in orthopyroxene as a function of pressure: a change of 6 wt % Al_2O_3 (2–8 wt %) causes a projected shift in X_{SiO_2} of 0·017 units (Spr–Opx tie-line in MAS), 0·034 units (Opx–Sil tie-line) and 0·025 units (Opx–Crd tie-line). (a) P–X_{SiO_2} diagram for the MAS reactions seen by Crn-bearing (Krn-absent) samples. The diagram has been drawn for the bulk composition of samples OG522A, OG522B, and OG524A, and a Mg/(Mg + Al) value of 0·66. (b) and (c) Semi-quantitative P–X_{SiO_2} diagrams for the MAS reactions seen by Krn-bearing samples at two nominal relative temperatures and drawn for B-present bulk compositions, and a Mg/(Mg + Al) value of 0·66. It should be noted that in Krn-bearing rocks, the Spr + Crd = Krn and Crn + Crd = Krn + Sil reactions are not 'seen' by bulk compositions that are less magnesian than the Crd–Krn tie-line. (b) Low T: temperatures between the [Spr Spl Grt] and [Spl Grt Crd] MAS invariant point. (c) High T: temperatures between the [Spl Grt Crd] and [Krn Crd Spl] MAS invariant point.

Kornerupine-present equilibria

The presence of kornerupine in the S_3 and S_4 assemblages in Pod 2 further constrains the P–T evolution of these rocks. The reaction and assemblage system being considered has to be expanded to include two new MAS invariant points, [Grt Spl Crd] and [Grt Spl Crn] (Fig. 12), generated from the [Grt Spl] MAS invariant from Fig. 9. This produces a kornerupine field, the size of which will be dependent, in the first instance, on Fe–Mg ratios in the ferromagnesian phases involved. More

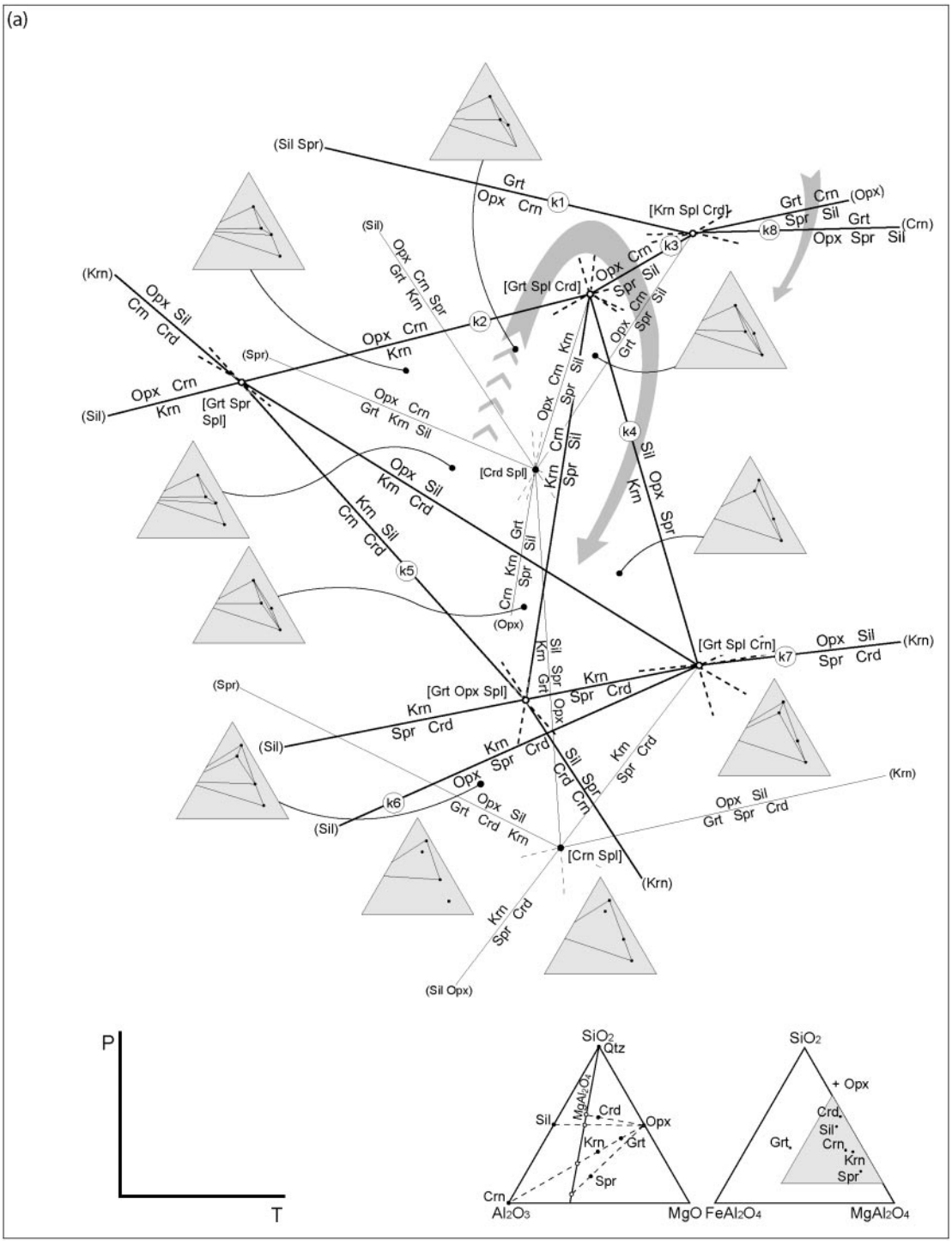

Fig. 12. (a) Qualitative *P–T* grid for the silica-undersaturated, kornerupine-bearing portion of the FMAS system. Thin lines are FMAS univariant reactions that may or may not terminate in MAS subsystem invariant points. Thicker lines are MAS invariants (FMAS divariants) constructed for assemblages observed in the Oygarden samples. Phases in FMAS compatibility diagrams are projected from orthopyroxene. It should be noted that Krn is assumed coplanar with Opx–Spr–Crd. Circled numbers on MAS univariant curves refer to reaction numbers discussed in the text. The estimated slopes of FMAS divariants k1, k3, k7, and k8 are equivalent to identical reactions in Fig. 9 (after Ouzegane *et al.*, 2003). The slope of reaction k2 is consistent with Wegge & Schreyer (1994). (b) MAS Schreinemakers' bundles that form parts of (a), with MAS compatibility triangles for reactions involving kornerupine. It should be noted that Krn is assumed collinear with Opx–Grt–Crn in MAS. (c) Schreinemakers' bundle for the [Crn Spl] FMAS invariant, indicating the change in topology if Krn is assumed to be more magnesian than the Opx–Spr–Crd plane in FMAS.

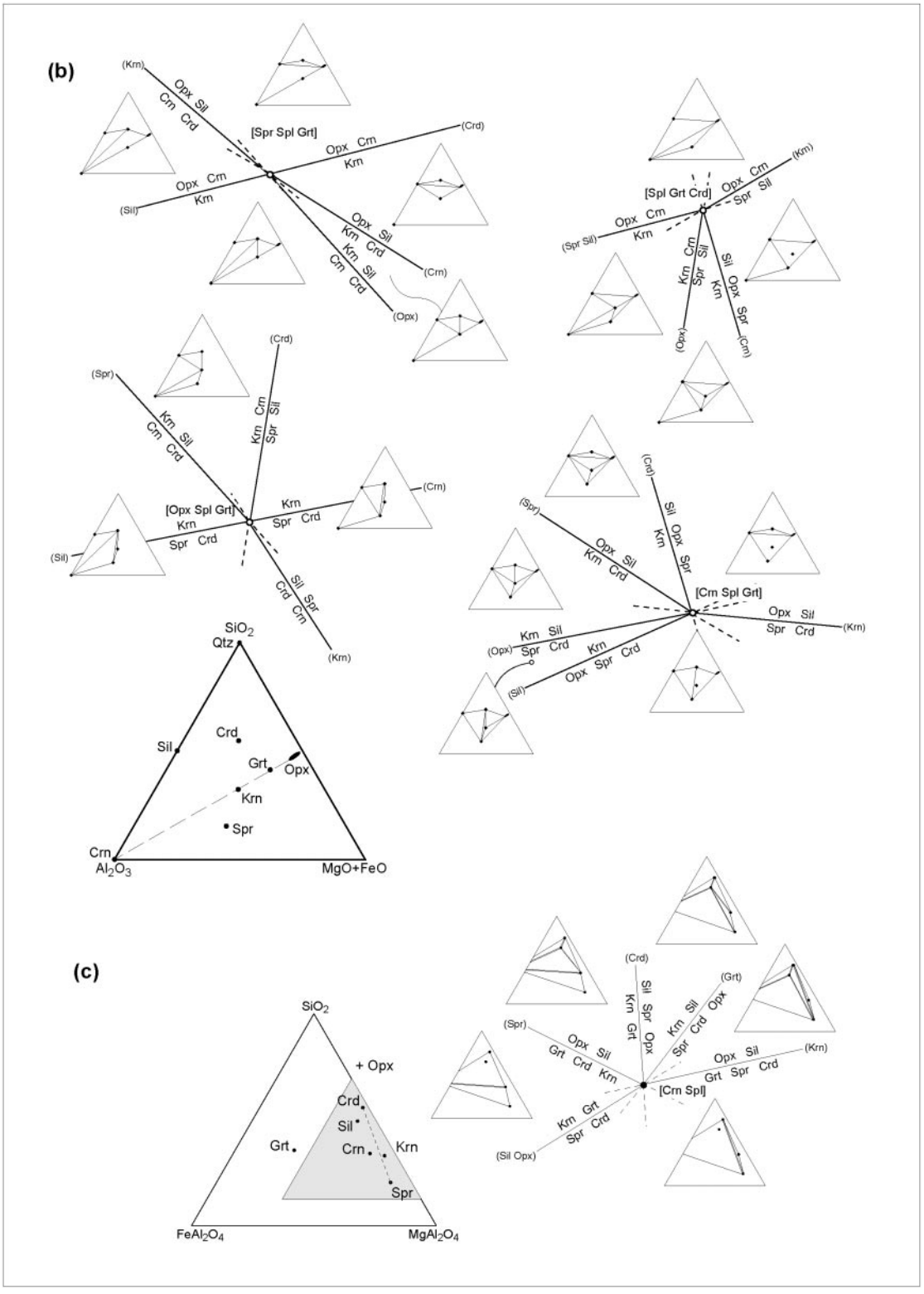

Fig. 12. Continued.

crucially, the kornerupine field and stability relations will depend on the B and H_2O (and F) content of the kornerupine involved. Increasing boron content in kornerupine will act to stabilize the kornerupine-present field, by shifting Krn-present invariant points and along Krn-absent univariants to higher pressures and temperatures (e.g. [Grt Spl Crn]), and to lower pressures (eg. [Grt Spl Crd]; Werding & Schreyer, 1996), with respect to its usual breakdown products that incorporate only minor or negligible B (Grew, 1996).

A qualitative, partial petrogenetic grid has been constructed for the minerals including garnet–orthopyroxene–sapphirine–corundum–kornerupine–sillimanite–cordierite in the simplified FMAS(B) system, centred on the [Crn Spl] and [Crd Spl] invariant points (Fig. 12a). The grid includes MAS terminations for selected reactions that are pertinent to the Oygarden assemblages and are discussed below. The topology of the FMAS univariant curves is determined by the [Krn Spl Crn] univariant reaction Opx + Sil = Grt + Spr + Crd. This reaction is equivalent to the [Krn Spl Qtz] univariant reaction and is constrained from the experiments and topological analysis of Hensen & Green (1973), Hensen (1986, 1987) and other workers (Bertrand *et al.*, 1991; Audibert *et al*, 1995; Carrington & Harley, 1995; Harley, 1998*b*) to have moderate, positive dP/dT slope, with orthopyroxene and sillimanite on the high-P side. The stability of B-free kornerupine in the grid is constrained by the experimental data of Wegge & Schreyer (1994). Reactions (k3), (k7) and (k8) are identical to reactions (2a), (2c) and (1a), respectively, from the [Krn] grid (Fig. 9) and have been given similar nominal slopes.

The topology of univariant reactions around the [Crn Spl] FMAS invariant point is largely controlled by the Fe–Mg composition of kornerupine and its position relative to the Opx–Spr–Crd plane in FMAS (Fig. 12a). The deviation of kornerupine from coplanarity with Opx–Spr–Crd as a result of differences in X_{Mg} is very small, and based on ambiguities surrounding the calculation of Fe^{3+} for the phases involved, it is reasonable to assume coplanarity to be the case. Figure 12a and b has therefore been calculated assuming this situation. The result of coplanarity between Opx–Spr–Crd–Krn is the generation of the degenerate reaction Krn = Spr + Crd [Sil Opx Grt] emanating from the [Crn Spl] FMAS invariant point. An alternative case, where kornerupine lies to the magnesian side of the Opx–Spr–Crd plane in FMAS, such as observed using average compositions for minerals from samples OG566 and OG567A when incorporating Fe^{3+} calculated using the cation/charge balance approach (Fig. 7e), is presented in Fig. 12c. This shift in composition results in changes to the [Grt Crn Spl], [Spr Crn Spl] and [Sil Crn Spl] FMAS univariants. No changes occur to reactions around the [Crd Spl] invariant point.

Based on textural evidence alone it is not clear exactly what sequence of reactions led to the formation of S_3 and S_4 kornerupine. However, indirect evidence can be taken from inclusion assemblages within or including kornerupine, and from equilibrium mineral associations. A number of potential kornerupine-forming reactions in this system can be considered, associated with the compositional sub-domains:

(1) core zone: garnet-poor or -absent assemblages, with inferred low X_{Si} and high X_{Mg};

(2) rind zone: garnet-present assemblages, with inferred lower X_{Mg} compared with (1) above.

In garnet-poor assemblages, garnet, corundum and sapphirine inclusions remain enclosed within S_3 kornerupine and orthopyroxene. Corundum inclusions are commonly separated from the kornerupine host by sapphirine. These textures are suggestive of an early period of garnet breakdown and also the reaction of corundum, possibly with orthopyroxene, early in D_3. A number of possible reaction scenarios at different P–T conditions can be considered. At low T ([Grt Spr Spl] < T < [Grt Spl Crd]), sequentially crossing reactions

$$\text{Grt} = \text{Opx} + \text{Crn} \qquad \text{(k1)}$$

and

$$\text{Opx} + \text{Crn} = \text{Krn} \qquad \text{(k2)}$$

could produce some of the observed inclusions assemblages. Alternatively, at higher temperatures ([Grt Spl Crd] < T < [Krn Spl Crd]), the inclusion assemblages may be produced by crossing reaction (k1) followed by the reactions

$$\text{Opx} + \text{Crn} = \text{Spr} + \text{Sil} \qquad \text{(k3)}$$

and

$$\text{Opx} + \text{Spr} + \text{Sil} = \text{Krn}. \qquad \text{(k4)}$$

At all temperatures, the suggested reactions [low T: reactions (k1) and (k2); high T: reactions (k3) and (k4)] will be crossed on a broadly decompressive P–T path.

The dominant S_3/S_4 assemblage of kornerupine, sapphirine and orthopyroxene may be stable over a broad P–T range (Fig. 12a), although is largely restricted to low X_{SiO_2} bulk compositions (dark shaded areas in Fig. 11b and c). At low T (Figs 11b and 12a) this assemblage is stable at pressures below reaction (k2). But at higher temperatures (T > [Grt Spl Crd]; Fig. 11c), kornerupine begins to break down with increasing pressure to the assemblage orthopyroxene–sapphirine–sillimanite at reaction (k4). Figure 11b and c suggests that for the restricted, relatively low X_{SiO_2} bulk composition of the Oygarden rocks, equilibration in the field bounded by

reactions (k2), (k4) and (k6) will produce the observed S_3 assemblage kornerupine–sapphirine–orthopyroxene. From the observed textures it is probable that decompression through this field, and/or equilibration in it, was responsible for the S_3 assemblages.

Garnet-present assemblages are inferred to have lower bulk X_{Mg} compositions compared with garnet-poor or -absent assemblages. S_3/S_4 kornerupine, sapphirine and orthopyroxene are inferred to have formed in a similar reaction sequence to those described above, but because of the increased stability of garnet with lower X_{Mg}, this probably occurred at lower pressures. The preservation of garnet embayed by kornerupine and orthopyroxene suggests decompression late in, or after, the development of S_4, possibly sequentially crossing a reaction similar to reaction (k8) and (k4) at low pressure. Alternatively, similar breakdown assemblages may be formed through a number of garnet-breakdown reactions described above, terminating in the orthopyroxene–sapphirine–kornerupine stability field. However, textural evidence for prior reactions is lacking.

Silica metasomatism and the effects of bulk-rock composition on assemblages

The combination of mineral and bulk-rock chemistry with assemblage and textural information illustrates the control that bulk composition exerts on assemblages and reaction products. For example, the modal abundance of sillimanite increases with increasing silica in the bulk composition of transition and rind zones. Similarly, although the appearance of cordierite in some zones is ultimately controlled by changes in pressure and temperature [reaction (2c); Figs 9 and 11a], cordierite is rare in the silica-poorer core zones. In addition, the percentage of progress of reaction (2a) is controlled by the X_{SiO_2} of each zone. A progressive increase in the extent of reaction occurs between the core, transition and rind zones, which is correlated with increasing X_{SiO_2}. This increase can be illustrated by comparing the size of reaction coronas in Fig. 2a–c. However, corundum is still preserved in the rind areas. This preservation also indicates that the process that led to the variation in bulk composition between zones is not likely to have occurred during the decompression phase of the RSE metamorphism, and that reaction textures developed in the rocks are not the result of metasomatic reactions. The slight enrichment of Fe and Si, and an apparent depletion in Mg, coupled with the increased abundance of phlogopite in the schistose rinds, suggests that the pods underwent fluid-assisted alteration at some stage in their history. However, if silica-metasomatism did occur during the development of the reaction textures, the orthopyroxene–corundum reactions would be expected to have gone to completion, leaving no relic corundum. In addition, the addition of a free silica phase in this outer zone may also be expected to produce aluminosilicate coronas on, or pseudomorphs after, corundum through a reaction such as $Crn + SiO_2 = Al_2SiO_5$. No evidence for this exists, therefore it is more likely that metasomatism occurred at least prior to the onset of decompression, and possibly prior to D_3 during the earlier Proterozoic or Archaean history of the rock.

The appearance of the stable high-pressure assemblage involving orthopyroxene and corundum is also, to a degree, dependent on the bulk composition. Figure 11a illustrates the restricted bulk compositions that can 'see' orthopyroxene and corundum. For the P–T conditions that the Oygarden rocks experienced, only bulk compositions with $X_{SiO_2} \approx 0{\cdot}35$–$0{\cdot}43$ will produce this assemblage. This figure also illustrates why spinel, a common constituent of high-Mg–Al metapelites, is absent from these assemblages. For the high-pressure conditions that accompanied metamorphism in the Oygarden Group, only bulk compositions with $X_{SiO_2} < 0{\cdot}35$ will produce spinel. However, spinel may form at lower pressure conditions than those inferred for the Oygarden Group. In addition to the variations discussed above, X_{SiO_2} is inferred to influence the products of garnet-breakdown reactions. For example, the bulk compositions of samples that preserve sillimanite-absent symplectites that formed after garnet plot between the garnet and orthopyroxene composition in MAS (Fig. 8d). Sample OG577, which preserves symplectites that contain both sillimanite and sapphirine, is more silica-rich in comparison with samples with no sillimanite, and plots closer to sillimanite in the MAS ternary diagram (Fig. 8c). Sample OG581 is the most silica-rich sample analysed, plotting above the orthopyroxene–sillimanite tie-line, and hence preserves no sapphirine. It is apparent that silica availability has to an extent controlled the product assemblages of these garnet-breakdown reactions.

The presence of boron

The occurrence of kornerupine in Pod 2 assemblage, and absence from all other pods investigated, is most certainly related to elevated boron in the bulk composition of Pod 2. Three models for the growth of kornerupine in these samples can be considered: (1) isochemical breakdown of a B-bearing phase; (2) addition to the system of a B-bearing fluid; or (3) primary bulk-rock controls (Waters & Moore, 1985; Carson *et al.*, 1995). There is no evidence in any samples for other B-bearing phases such as tourmaline as either inclusions or mineral relics from which the B may be sourced. This suggests that the breakdown of a B-phase was probably not responsible for the production of kornerupine. The pods show ample evidence for

metasomatism during an earlier phase of metamorphism, so it could be argued that kornerupine may form through reaction involving a B-bearing fluid (Waters & Moore, 1985). There are no bulk-rock data for Pod 2. However, kornerupine is evenly distributed throughout Pod 2, and not restricted to the schistose rinds and transition zones. It is therefore likely that boron was not introduced during the metasomatic event that produced the dominant zoning that is described in detail in this paper. It is therefore likely that boron was present in the pre-D_3/D_4 bulk composition (in low abundance in typically B-free minerals) either as a primary compositional variation from the other rocks from which the pods were sourced or as the result of a previous alteration event.

Prograde and retrograde garnet stability

The increase in size and abundance of garnet in the outer zones and rinds of the pods can be correlated directly with differences in garnet chemistry. Garnet X_{Pyp} values are lower in rind areas than in cores, and can differ by as much as $X_{Pyp} = 0{\cdot}16$. In addition, lower X_{Pyp} values correlate with higher garnet abundances and grain size. Pod 10, which is garnet-rich in comparison with other pods, also preserves garnet grains that are higher in X_{Grs} (up to 0·06). Moreover, the bulk-rock compositions of samples from Pod 10 commonly have higher CaO contents. The textural context of the metasomatic zones is interpreted to reflect a bulk compositional zoning profile that existed prior to D_4, and most probably before D_3. Therefore variations in garnet compositions between zones reflect an initial bulk-rock composition and not changes caused by Fe–Mg exchange or metasomatism during metamorphism.

Garnet inclusions in S_3 sapphirine and kornerupine suggest that D_3 garnet growth during a prograde pressure increase was followed by a period of garnet breakdown. Garnet breakdown is interpreted to have been the result of decompression from peak pressures. This decompression during the D_3 event would have allowed growth of S_3 sapphirine and kornerupine with inclusions of garnet. Symplectites that replace garnet and overgrow S_4 in garnet-rich rocks imply that further garnet breakdown occurred during continued decompression late in D_4. These two apparent stages of garnet breakdown can be correlated with the Mg and, to a lesser extent, Ca contents of the garnet grains from the different zones. Garnet grains with high X_{Pyp} values mainly occur as inclusions in S_3 sapphirine and kornerupine, and broke down early in the decompression path. Garnet grains with less magnesian compositions, for example those located in the transition zones and rinds, are more commonly preserved in the S_3 assemblage as small garnet relics. This garnet probably began to break down late in D_3 or early in D_4. Breakdown of garnet grains that are now preserved as larger, embayed porphyroblasts produced symplectites that overprint S_4 and therefore are interpreted to have occurred late in D_4. Preservation of larger garnet grains in the rind zones is therefore a result of higher Fe contents displacing the garnet-present equilibria [e.g. reaction (1a); Fig. 9] to lower pressures. This may also explain the relative abundances of garnet in different samples, as prograde garnet would probably have formed at lower pressures in samples with higher Fe contents than in samples with higher Mg contents. This garnet would in turn be consumed at lower pressures on the decompression path.

Equilibrium assemblage: orthopyroxene and corundum

In corundum-bearing samples, corundum is commonly separated from orthopyroxene by reaction rims of sapphirine, sapphirine + sillimanite, or sapphirine + cordierite (Fig. 3). In the case of mono-mineralic sapphirine coronas, these rims can be narrow and mimic the grain boundaries of the corundum (Fig. 3a). The widths of these coronas are much less than the size of the grains that they separate. Moreover, several orthopyroxene grains may be adjacent to any one corundum grain, suggesting that corundum does not occur as metastable inclusions in orthopyroxene. This texture implies that textural, if not chemical, equilibrium was attained between orthopyroxene and corundum in the Oygarden rocks prior to reaction. This assemblage has been previously proposed to exist from chemographic and topological requirements by Hensen (1986, 1987) and Waters (1986), and also from experimental evidence (Ackermand, 1970). Morse & Talley (1971) reported orthopyroxene + corundum (+ spinel) amongst the breakdown products of sapphirine + quartz (Wilson Lake, Labrador), and interpreted the association to reflect a high-P instability of sapphirine + magnetite. Grew (1983) also reported from Enderby Land (East Antarctica) the occurrence of corundum within sillimanite coronae around sapphirine, where orthopyroxene formed further coronae around sillimanite, but did not infer stability of the orthopyroxene–corundum association in these rocks. In addition, Motoyoshi *et al.* (1990) inferred orthopyroxene + corundum as reaction products after sapphirine + quartz breakdown during apparent isobaric cooling. Other workers have inferred prior equilibrium between orthopyroxene and corundum (e.g. Windley *et al.*, 1984; Bertrand *et al.*, 1992; Goscombe, 1992; Kihle & Bucher-Nurminen, 1992), usually on the basis of small grains that are not always in proximity to orthopyroxene, or from inclusion assemblages (Kriegsman & Schumacher, 1999). Recently, more convincing evidence was presented by

Ouzegane *et al.* (2003), who reported the extensive development of sapphirine + sillimanite coronae armouring corundum, with sapphirine + cordierite coronae separating sillimanite from orthopyroxene. Ouzegane *et al.* (2003) inferred orthopyroxene–corundum breakdown through prograde heating at $P \approx 10$ kbar. These textures form a similar sequence to that reported here for the Oygarden Group metapelites. However, the Oygarden rocks are one of the clearest examples of orthopyroxene–corundum stability that we are aware of, proving that this assemblage can occur in natural systems.

This rare association is predicted to occur only in rocks with a restricted bulk-rock composition metamorphosed under restricted P–T conditions. Grew (1983) suggested that the reaction orthopyroxene + corundum = garnet + sapphirine + sillimanite reflected the upper temperature limit of the assemblage (as indicated in Fig. 9 of this study). In addition, conditions of $P = 9$–$11{\cdot}5$ kbar and $T = 750$–850°C (above the kyanite–sillimanite univariant curve) with low water activities were inferred to be required to stabilize the assemblage (Grew, 1983). Currently available thermodynamic data also indicate that the rocks must pass through, or equilibrate at, moderately high pressures of $P > 11$ kbar (for the MAS system) or slightly lower for rocks with lower X_{Mg}. The Oygarden rocks suggest that this assemblage formed at conditions of $P > 10$ kbar and $T = 800$–850°C. The restricted P–T range within which orthopyroxene and corundum will coexist means that this assemblage is unlikely to be preserved in most circumstances. During the later stages of typical clockwise P–T paths, characterized by decompression after peak metamorphic conditions, this assemblage easily reacts to produce assemblages involving orthopyroxene, sapphirine, and sillimanite or cordierite, or to form kornerupine-bearing assemblages. Anti-clockwise P–T paths, preserved in a number of granulite terranes, are unlikely to intersect conditions appropriate for orthopyroxene–corundum stability. However, in this situation this assemblage may form through reaction between sapphirine and sillimanite if the sapphirine involved has high Mg content, and the cooling path passed through $T \approx 800$–850°C at $P > 8$–10 kbar. This circumstance may be rare.

P–T–t PATH FOR KEMP LAND

The sequence of kornerupine-absent and -present equilibria described above can be coupled to establish a clockwise P–T–t evolution for the Oygarden Group of islands during the Rayner Structural Episode (Fig. 10).

Prograde history and initial decompression

The S_3 assemblages, including kornerupine, orthopyroxene and sapphirine, record increasing pressure through the kornerupine stability field (Figs 9 and 11) to reach peak pressures of up to 10–11 kbar, and possibly higher. This pressure increase reflects tectonic thickening of the terrane during D_3 thrusting that occurred in an overall transpressional setting (Kelly *et al.*, 2000). It is unclear at what crustal level this part of Kemp Land resided prior to the RSE. However, coarse-grained garnet coronas and 'necklaces' in mafic granulites that are also embayed by post-D_3 reaction textures (Kelly, 2000) suggest that thickening did in fact occur, and the S_3 assemblages described here do not simply reflect thrust-related activation of the middle to lower continental crust.

Garnet inclusions in S_3 sapphirine and kornerupine are consistent with garnet breakdown subsequent to peak pressures being attained. These textures are interpreted to result from crossing one or more reactions that emanate from the [Crd Sil] or the [Crd Spl] MAS invariants (Fig. 9), and reactions (k1), (k2) or (k8) in kornerupine-bearing rocks (Fig. 12). These reactions reflect a phase of decompression that commenced during D_3, with peak pressures reached prior to the thermal maximum. Corundum with sapphirine coronas included in kornerupine also suggests that reactions (k3) and (k4) may have been crossed with decreasing pressure. This P–T path is on the high-T side of the [Grt Spl Crd] invariant point in the Krn-present grid, implying that early decompression from peak D_3 pressures above the [Grt Spl Crd] point was accompanied by a rise in temperature late in D_3 or during D_4, followed by minor cooling across reaction (k4).

The continued heating of the Oygarden terrane, or at least residence at high temperatures during D_3 and D_4, is reflected in the grain size and texture of thrust zones. D_3 thrust zones are typically not mylonitic in texture but instead are coarse-grained, suggesting that deformation was characterized by a slow strain rate or the thrust zones were annealed following deformation (Kelly *et al.*, 2000). The latter interpretation is consistent with a period of higher temperatures following D_3. Based on the experimentally constrained KFMASH grid (Hensen & Green, 1973; Carrington & Harley, 1995), fine-grained intergrowths of orthopyroxene, sillimanite and quartz after garnet and biotite in quartz-present metapelites (Kelly, 2000) indicate that peak temperatures may have exceeded 900°C for a limited period of time. The absence of ultrahigh-temperature assemblages, for example the association sapphirine + quartz, provides a limit to peak temperatures achieved, such that the temperature rise during decompression was probably not greater than 100°C.

Post-peak decompression

Reaction textures between orthopyroxene and corundum in kornerupine-absent rocks are interpreted to represent decompression across reactions (2a) and (2c) (Fig. 9) during D_4. The slope of reaction (2a) is not well constrained

experimentally, and it is possible that this reaction is crossed through heating (e.g. Bertrand *et al.*, 1992) or decompression with either rising or falling temperature. Reaction (2c), in corundum-bearing rocks, has a shallow, positive slope. The products of this reaction are commonly fine-grained with respect to the reactant phases, so it is realistic to assume that these reactions were crossed as a result of decompression. Assemblages from kornerupine-bearing rocks suggest that this may have followed, or was accompanied by, minor heating to conditions above those appropriate to [Grt Spl Crd]. Furthermore, garnet breakdown textures that overgrew S_4 reflect decompression across reaction (1a) late in, or following, D_4. Reactions (1a) and (2a), which occur at different relative pressures and temperatures (Fig. 9), appear to have occurred in different rocks during the same period of decompression. This contradiction can be explained by differences in bulk-rock compositions and the resulting phase compositions, which are inferred to displace these equilibria a considerable distance in P–T space.

Although no quantitative pressure estimates could be made for the reaction textures developed in these rocks, estimates from mafic gneiss (Kelly, 2000; Kelly *et al.*, 2000), and estimates made for reaction textures in mafic gneiss from elsewhere in Kemp Land (Else Nunataks, *c.* 80 km SW of the Oygarden Group; Pieters & Wyborn, 1977; Ellis, 1983), suggest that decompression from $P \approx 10$ kbar to $P \approx 5$ kbar occurred during and after D_4. This exhumation, which was initially triggered during D_3 thrusting, is inferred to have continued during the shift from thrusting to extension during D_4. This latter event is characterized in the Oygarden Group by a 2–3 km crustal-scale shear zone. The coarse-grained nature of rocks reflects a degree of annealing of mylonitic textures following cessation of movement on this shear zone, and suggests the possibility of as yet unidentified structures controlling the continued exhumation of the terrane.

Mineral assemblages that characterize S_3 and S_4 in the silica-undersaturated rocks are commonly similar and of similar grain size. Moreover, the grain sizes of minerals that are involved in the reaction textures that developed during D_3 are similar to, or larger than, those that developed later in D_4. The post-D_4 textures are commonly appreciably smaller in grain size than the peak mineral assemblages that they overprint. This suggests that the textures did not form purely by heating, which would produce later textures that were coarser in grain size, or completely overprint the earlier textures. Therefore the reaction textures described here did not form as a result of a second metamorphic event at lower pressures but are consistent with a single metamorphic/orogenic cycle. This continuous clockwise P–T path was dominated by decompression and accompanied by a minor component of heating. Age estimates for D_3 and D_4 overlap (*c.* 930–900 Ma; Kelly *et al.*, 2002), supporting this interpretation.

Kemp Land within the Rayner Complex

The characterization in Kemp Land of a clockwise P–T trajectory dominated by post-peak decompression (Pieters & Wyborn, 1977; Ellis; 1983; this study) contrasts markedly with P–T paths recorded elsewhere in the Rayner Complex. Reaction textures in rocks from the Mawson Coast are interpreted to be consistent with an anticlockwise P–T path with isobaric cooling after the peak of metamorphism (Clarke *et al.*, 1989; Dunkley *et al.*, 2003). In the Stillwell Hills, an early phase of apparent cooling may have preceded decompression (Clarke, 1987; Harley & Hensen, 1990) and is similar to the P–T path recorded by rocks in the northern Prince Charles Mountains (Fitzsimons & Thost, 1992; Thost & Hensen, 1992; Hand *et al.*, 1994; Nichols, 1995). More recent work (Boger & White, 2003) has suggested an anticlockwise P–T path dominated by retrograde cooling for the northern Prince Charles Mountains.

These differences may be linked to the relative timing of metamorphism and/or the location of these areas with respect to contraction across the orogen. Sheraton *et al.* (1987) suggested that areas that preserve lower-pressure assemblages, such as MacRobertson Land and the northern Prince Charles Mountains, record the later stages of the metamorphic event, and the areas that preserve higher-pressure assemblages, such as Kemp Land, record only the earlier, high-pressure part of the event. The higher-pressure rocks were interpreted to have been exhumed by thrusting over the Napier Complex, so were not recrystallized at lower pressures (Sheraton *et al.*, 1987; Harley & Hensen, 1990). However, isotopic data from the Oygarden area indicate that thrusting and high-pressure granulite-facies metamorphism affected Kemp Land between *c.* 0·93 and 0·90 Ga (Kelly *et al.*, 2002), after the low-P, high-T event in MacRobertson Land that is interpreted to have occurred between *c.* 0·99 and 0·97 Ga (Manton *et al.*, 1992; Kinny *et al.*, 1997; Boger *et al.*, 2000; Dunkley *et al.*, 2003). Therefore, the earliest deformation in MacRobertson Land does not correlate with that seen in Kemp Land, and the isobaric cooling event in MacRobertson Land cannot be directly compared with the isothermal decompression event in Kemp Land. Interestingly, a second phase of metamorphism and deformation, correlated with a complex-wide shift from broadly contractional to transpressional tectonism, affected the Rayner Complex of MacRobertson Land between *c.* 0·94 and 0·90 Ma (Young & Black, 1991; Manton *et al.*, 1992; Boger *et al.*, 2000; Carson *et al.*, 2001; Dunkley *et al.*, 2003). Apparent decompression inferred from rocks of the northern Prince Charles Mountains (Hand *et al.*, 1994; Nichols, 1995) is probably related to this later event, the age of which correlates with the dominant phase of metamorphism and deformation in Kemp Land.

CONCLUSIONS

The high-Al–Mg rocks described here contain textural evidence for the existence in nature of the stable assemblage involving orthopyroxene and corundum. This assemblage has been previously proposed to exist from chemographic and topological requirements, from experimental evidence and on the basis of reaction textures and inclusion assemblages. Textural evidence in the Oygarden rocks shows that this mineral assemblage was stable, and will occur as a stable assemblage only in rocks with a restricted bulk-rock composition ($X_{SiO_2} = 0{\cdot}35$–$0{\cdot}43$ for high-magnesian rocks) metamorphosed under restricted P–T and low water activity conditions. For these compositions, moderately high pressures of $P >$ 11 kbar are required (for the MAS system) or slightly lower for rocks with higher X_{Fe}. In the Oygarden rocks, this assemblage formed at conditions of $P >$ 9 kbar and $T = 800$–$850°C$. At pressures below this, assemblages will develop minerals including sapphirine, sillimanite and cordierite with orthopyroxene; at much higher pressures ($P >$ 13 kbar) orthopyroxene and corundum will react to form garnet; and at lower temperatures, or if boron is present, late kornerupine will develop. The restricted P–T range within which orthopyroxene and corundum can coexist means that this assemblage is unlikely to be preserved in most circumstances.

The reaction grid presented to describe textures from the Oygarden Group silica-undersaturated metapelites differs from previously published grids by ignoring gedrite and spinel, instead focusing on the high-pressure reactions. The grid presents FMAS univariant reactions linked to MAS terminations and divariant equilibria, and incorporates and satisfies the topology of the [Krn Spl Crn] univariant reaction and the kornerupine-present experimental results of Wegge & Schreyer (1994). The integration of assemblage and reaction texture information with the reaction grid allows the definition of a clockwise P–T path that reached peak pressures of $P \approx$ 9–10 kbar prior to a thermal maximum. Initial decompression was accompanied by thermal relaxation of the crust toward peak temperatures of up to $T \approx 850$–$900°C$ and continued decompression. The clockwise isothermal decompression path recorded by Kemp Land contrasts with elsewhere in the Rayner Complex, and is interpreted to correlate with the second phase of tectonism to affect MacRobertson Land.

ACKNOWLEDGEMENTS

This work was completed with funding from the Antarctic Science Advisory Committee (Geoff L. Clarke and S.L.H.; ASAC Project No. 2214). Fieldwork was conducted during the 1996–1997 and 1997–1998 Australian National Antarctic Research Expeditions. The Australian Antarctic Division and the personnel of Mawson Base are thanked for logistic support. Part of this work was completed while N.M.K. was a postgraduate student visitor at the University of Edinburgh, with the assistance of an Edgeworth David Travel Grant-In-Aid (University of Sydney). N.M.K. also acknowledges the support of a University of Sydney Postgraduate Research Award (1996–2000) and a Royal Society of Edinburgh SEELLD Personal Fellowship (2001–). XRF analyses were funded by a Royal Society Grant to S.L.H. Drs Peter Hill and Nicola Cayzer are thanked for assistance with the electron probe and scanning electron microscope (University of Edinburgh); Barry Searle (UNSW) is thanked for his assistance with electron probe and element map analysis. Nathan Daczko is thanked for help with element map processing. SIMS analyses of kornerupine were performed with the assistance of Richard Hinton at the University of Edinburgh. Chris Carson, Julie Hollis, Richard White and Venessa Bennett are thanked for assistance in the field, and Geoff Clarke is thanked for editing an early version of this manuscript. The authors would also like to thank E. S. Grew, K. K. Podlesskii and V. N. Balashov for thorough and constructive reviews, and L. L. Perchuk for editorial assistance.

SUPPLEMENTARY DATA

Supplementary data for this paper are available at *Journal of Petrology* online.

REFERENCES

Ackermand, D. (1970). Stabilitat und Synthese des Sapphirins im System MgO–Al_2O_3–SiO_2–(H_2O). Ph.D. thesis, Bochum University, 97 pp.

Aranovitz, L. Y. & Berman, R. G. (1997). A new garnet–orthopyroxene barometer based on reversed Al_2O_3 solubility in FeO–Al_2O_3–SiO_2 orthopyroxene. *American Mineralogist* **82**, 345–353.

Audibert, N., Hensen, B. J. & Bertrand, P. (1995). Experimental study of phase relations involving osumulite in the system K_2O–FeO–MgO–Al_2O_3–SiO_2–H_2O at high pressure and temperature. *Journal of Metamorphic Geology* **13**, 331–344.

Bence, A. E. & Albee, A. L. (1968). Empirical correction factors for the electron microanalysis of silicates and oxides. *Journal of Geology* **76**, 382–403.

Berman, R. G., Brown, T. H. & Greenwood, H. J. (1985). An internally consistent thermodynamic data base for minerals in the system Na_2O–K_2O–CaO–MgO–FeO–SiO_2–Al_2O_3–Fe_2O_3–TiO_2–H_2O–CO_2. *Atomic Energy Canada Ltd, Technical Report* TR-377.

Bertrand, P., Ellis, D. J. & Green, D. H. (1991). The stability of sapphirine–quartz and hypersthene–sillimanite–quartz assemblages: an experimental investigation in the system FeO–MgO–Al_2O_3–SiO_2 under H_2O and CO_2. *Contributions to Mineralogy and Petrology* **108**, 55–71.

Bertrand, P., Ouzegane, K. & Kienast, J. R. (1992). P–T–X relationships in the Precambrian Al–Mg-rich granulites from In Ouzzal, Hoggar, Algeria. *Journal of Metamorphic Geology* **10**, 17–31.

Boger, S. D. & White, R. W. (2003). The metamorphic evolution of metapelitic granulites from Radok Lake, northern Prince Charles Mountains, east Antarctica; evidence for an anticlockwise *P–T* path. *Journal of Metamorphic Geology* **21**, 285–298.

Boger, S. D., Carson, C. J., Wilson, C. J. L. & Fanning, C. M. (2000). Neoproterozoic deformation in the Radok Lake region of the northern Prince Charles Mountains, east Antarctica; evidence for a single protracted orogenic event. *Precambrian Research* **104**, 1–24.

Carrington, D. P. & Harley, S. L. (1995). Partial melting and phase relations in high-grade metapelites: an experimental petrogenetic grid in the KFMASH system. *Contributions to Mineralogy and Petrology* **120**, 270–291.

Carson, C. J., Hand, M. & Dirks, P. H. G. M. (1995). Stable coexistence of grandidierite and kornerupine during medium pressure granulite facies metamorphism. *Mineralogical Magazine* **59**, 327–339.

Carson, C. J., Boger, S. D., Fanning, C. M., Wilson, C. J. L. & Thost, D. E. (2001). SHRIMP U–Pb geochronology from Mt Kirkby, northern Prince Charles Mountains, east Antarctica. *Antarctic Science* **12**, 429–442.

Clarke, G. L. (1987). A comparative study of the structural and metamorphic evolution of the Olary (South Australia) and Stillwell Hills (Antarctica) Precambrian terrains. Ph.D. thesis, University of Melbourne, 254 pp.

Clarke, G. L., Powell, R. & Guiraud, M. (1989). Low-pressure granulite facies metapelitic assemblages and corona textures from MacRobertson Land, east Antarctica: the importance of Fe_2O_3 and TiO_2 in accounting for spinel-bearing assemblages. *Journal of Metamorphic Geology* **7**, 323–335.

Clarke, G. L., Daczko, N. & Nockolds, C. (2001). A method for applying matrix corrections to X-ray intensity maps using the Bence–Albee algorithm and Matlab. *Journal of Metamorphic Geology* **19**, 635–644.

Deer, W. A., Howie, R. A. & Zussman, J. (1992). *An Introduction to the Rock Forming Minerals*. Harlow: Longman, 696 pp.

Droop, G. T. R. (1989). Reaction history of garnet–sapphirine granulites and conditions of Archaean high-pressure granulite-facies metamorphism in the Central Limpopo Mobile Belt, Zimbabwe. *Journal of Metamorphic Geology* **7**, 383–403.

Droop, G. T. R. & Bucher-Nurminen, K. (1984). Reaction textures and metamorphic evolution of sapphirine-bearing granulites from the Gruf Complex, Italian Central Alps. *Journal of Petrology* **25**, 766–803.

Dunkley, D. J., Clarke, G. L. & Harley, S. L. (1999). Diffusion metasomatism in silica-undersaturated sapphirine-bearing granulite from Rumdoodle Peak, Framnes Mountains, east Antarctica. *Contributions to Mineralogy and Petrology* **134**, 264–276.

Dunkley, D. J., Clarke, G. L. & White R. W. (2003). The *c*. 1020–900 Ma Rayner Structural Episode in MacRobertson Land, east Antarctica: a case of oblique continental collision? *Proceedings of the 8th International Symposium on Antarctic Earth Sciences, Wellington, New Zealand, 1999. Royal Society of New Zealand Bulletin* **35**, 31–42.

Ellis, D. J. (1983). The Napier and Rayner Complexes of Enderby Land, Antarctica—contrasting styles of metamorphism and tectonism. In: Oliver, R. L., James, P. R. & Jago, J. B. (eds) *Antarctic Earth Science*. Canberra, A.C.T.: Australian Academy of Science, pp. 20–24.

Fitzsimons, I. C. W. & Harley, S. L. (1994). The influence of retrograde cation exchange on granulite *P–T* estimates and a convergence technique for the recovery of peak metamorphic conditions. *Journal of Metamorphic Geology* **12**, 411–428.

Fitzsimons, I. C. W. & Thost, D. E. (1992). Geological relationships in high-grade basement gneiss of the northern Prince Charles Mountains, east Antarctica. *Australian Journal of Earth Sciences* **39**, 173–193.

Friend, C. R. L. (1995). Occurrences of boron-free and boron-poor kornerupine. *Mineralogical Magazine* **59**, 163–166.

Ganguly, J., Cheng, W. & Tirone, M. (1996). Thermodynamics of aluminosilicate garnet solid solution: new experimental data, an optimized model, and thermometric applications. *Contributions to Mineralogy and Petrology* **126**, 137–151.

Gasparik, T. & Newton, R. C. (1984). The reversed alumina contents of orthopyroxene in equilibrium with spinel and forsterite in the system $MgO–Al_2O_3–SiO_2$. *Contributions to Mineralogy and Petrology* **85**, 186–196.

Goscombe, B. (1992). Silica-undersaturated sapphirine, spinel and kornerupine granulite facies rocks, NE Strangeways Range, central Australia. *Journal of Metamorphic Geology* **10**, 181–201.

Grew, E. S. (1983). Sapphirine–garnet and associated parageneses in Antarctica. In: Oliver, R. L., James, P. R. & Jago, J. B. (eds) *Antarctic Geoscience*. Canberra, A.C.T.: Australian Academy of Science, pp. 40–43.

Grew, E. S. (1996). Borosilicates (exclusive of tourmaline) and boron in rock-forming minerals in metamorphic environments. In: Grew, E. S. & Anovitz, L. M. (eds) *Boron: Mineralogy, Petrology and Geochemistry*. *Mineralogical Society of America, Reviews in Mineralogy* **33**, 387–480.

Grew, E. S., Manton, W. I. & James, P. R. (1988). U–Pb data on granulite facies rocks from Fold Island, Kemp Coast, east Antarctica. *Precambrian Research* **42**, 63–75.

Grew, E. S., Redhammer, G. J., Amthauer, G., Cooper, M. A., Hawthorne, F. C. & Schmetzer, K. (1999). Iron in kornerupine: a ^{57}Fe Mössbauer spectroscopic study and comparison with single-crystal refinement. *American Mineralogist* **84**, 536–549.

Hand, M., Scrimgeour, I., Powell, R., Stuwe, K. & Wilson, C. J. L. (1994). Metapelitic granulites from Jetty Peninsula, east Antarctica: formation during a single event or by polymetamorphism? *Journal of Metamorphic Geology* **12**, 557–573.

Harley, S. L. (1993). Sapphirine granulites from the Vestfold Hills, East Antarctica: geochemical and metamorphic evolution. *Antarctic Science* **5**, 389–402.

Harley, S. L. (1998*a*). Ultrahigh temperature granulite facies metamorphism (1050°C, 12 kbar) and decompression in garnet (Mg70)–orthopyroxene–sillimanite gneisses from the Rauer Goup, East Antarctica. *Journal of Metamorphic Geology* **16**, 541–562.

Harley, S. L. (1998*b*). On the occurrence and characterisation of ultrahigh-temperature crustal metamorphism. In: Treloard, P. J. & O'Brien, P. J. (eds) *What Drives Metamorphism and Metamorphic Reactions? Geological Society, London, Special Publications* **138**, 81–107.

Harley, S. L. & Black, L. P. (1997). A revised Archaean chronology for the Napier Complex, Enderby Land, from SHRIMP ion-microprobe studies. *Antarctic Science* **9**, 74–91.

Harley, S. L. & Green, D. H. (1982). Garnet–orthopyroxene barometry for granulites and peridotites. *Nature* **300**, 697–701.

Harley, S. L. & Hensen, B. J. (1990). Archaean and Proterozoic high-grade terranes of east Antarctica (40–80°): a case study of diversity in granulite facies metamorphism. In: Ashworth, J. R. & Brown, M. (eds) *High-temperature Metamorphism and Crustal Anatexis*. *Mineralogical Society Special Publications* **2**, 320–370.

Harley, S. L. & Motoyoshi, S. L. (2000). Al zoning in orthopyroxene in a sapphirine quartzite: evidence for >1120°C UHT metamorphism in the Napier Complex, Antarctica, and implications for the entropy of sapphirine. *Contributions to Mineralogy and Petrology* **138**, 293–307.

Hensen, B. J. (1971). Theoretical phase relations involving cordierite and garnet in the system, $MgO–FeO–Al_2O_3–SiO_2$. *Contributions to Mineralogy and Petrology* **3**, 191–214.

Hensen, B. J. (1986). Theoretical phase relations involving garnet and cordierite revisited: the influence of oxygen fugacity on the stability

of sapphirine and spinel in the system Mg–Fe–Al–Si–O. *Contributions to Mineralogy and Petrology* **92**, 191–214.

Hensen, B. J. (1987). *P–T* grids for silica-undersaturated granulites in the systems MAS ($n + 4$) and FMAS ($n + 3$)—tools for the derivation of *P–T* paths of metamorphism. *Journal of Metamorphic Geology* **5**, 255–271.

Hensen, B. J. & Green, D. H. (1973). Experimental study of the stability of cordierite and garnet in pelitic compositions at high pressures and temperatures. III. Synthesis of experimental data and geological applications. *Contributions to Mineralogy and Petrology* **38**, 151–166.

Hinton, R. W. (1995). Ion microprobe analysis in geology. In: Reed, S. J. B. & Potts, P. J. (eds) *Microanalytical Techniques*. London: Chapman & Hall, pp. 235–289.

Holland, T. J. B. & Powell, R. (1998). An internally consistent thermodynamic dataset for phases of petrological interest. *Journal of Metamorphic Geology* **16**, 309–343.

Kelly, N. M. (2000). Deformation and metamorphism in the lower continental crust: Oygarden Group of Islands, east Antarctica. Ph.D. thesis, University of Sydney, 287 pp.

Kelly, N. M., Clarke, G. L., Carson, C. J. & White, R. W. (2000). Thrusting in the lower crust: evidence from the Oygarden Islands, Kemp Land, East Antarctica. *Geological Magazine* **137**, 219–234.

Kelly, N. M., Clarke, G. L. & Fanning, C. M. (2002). A two-stage evolution of the Neoproterozoic Rayner Structural Episode: new U–Pb sensitive high resolution ion microprobe constraints from the Oygarden Group, Kemp Land, East Antarctica. *Precambrian Research* **116**, 307–330.

Kihle, J. & Bucher-Nurminen, K. (1992). Orthopyroxene–sillimanite–sapphirine granulites from the Bamble granulite terrane, southern Norway. *Journal of Metamorphic Geology* **10**, 671–683.

Kinny, P. D., Black, L. P. & Sheraton, J. W. (1997). Zircon U–Pb ages and geochemistry of igneous and metamorphic rocks from the northern Prince Charles Mountains, Antarctica. *AGSO Journal of Australian Geology and Geophysics* **16**, 637–654.

Kretz, R. (1983). Symbols for rock-forming minerals. *American Mineralogist* **68**, 277–279.

Kriegsman, L. M. & Schumacher, J. C. (1999). Petrology of sapphirine-bearing and associated granulites from central Sri Lanka. *Journal of Petrology* **40**, 1211–1239.

Manton, W. I., Grew, E. S., Hofmann, J. & Sheraton, J. W. (1992). Granitic rocks of the Jetty Peninsula, Amery Ice Shelf area, east Antarctica. In: Yoshida, Y., Kaminuma, K. & Shiraishi, K. (eds) *Recent Progress in Antarctic Earth Science*. Tokyo: Terra, pp. 179–189.

Moore, P. B. (1969). The crystal structure of sapphirine. *American Mineralogist* **54**, 21–49.

Morse, S. A. & Talley, J. H. (1971). Sapphirine reactions in deep-seated granulites near Wilson Lake, central Labrador, Canada. *Earth and Planetary Science Letters* **10**, 325–328.

Motoyoshi, Y., Hensen, B. J. & Matsueda, H. (1990). Metastable growth of corundum adjacent to quartz in a spinel-bearing quartzite from the Napier Complex, Antarctica. *Journal of Metamorphic Geology* **8**, 125–130.

Motoyoshi, Y., Ishikawa, M. & Fraser, G. L. (1995). Sapphirine-bearing silica-undersaturated granulites from Forefinger Point, Enderby Land, East Antarctica: evidence for a clockwise *P–T* path? *Proceedings of the NIPR Symposium on Antarctic Geosciences* **8**, 121–129.

Newton, R. C. (1972). An experimental determination of the high pressure stability limits of magnesian cordierite under wet and dry conditions. *Journal of Geology* **80**, 398–420.

Nichols, G. T. (1995). The role of mylonites in the uplift of an oblique lower crustal section, east Antarctica. *Journal of Metamorphic Geology* **13**, 223–238.

Ouzegane, K., Guiraud, M. & Kienast, J. R. (2003). Prograde and retrograde evolution in high-temperature corundum granulites (FMAS and KFMASH systems) from In Ouzzal Terrane (NW Hoggar, Algeria). *Journal of Petrology* **44**, 517–545.

Pieters, P. E. & Wyborn, D. (1977). Geological work in Antarctica—1974/75. *Bureau of Mineral Resources, Australia, Record* 1977/16 (unpublished).

Pouchou, L. & Pichoir, F. (1984). A new model for quantitative X-ray microanalysis. *Recherche Aerospatiale* **3**, 167–192.

Powell, R. & Holland, T. J. B. (1988). An internally consistent dataset with uncertainties and correlations: 3. Applications to geobarometry, worked examples and a computer program. *Journal of Metamorphic Geology* **6**, 173–204.

Sandiford, M. & Wilson, C. J. L. (1984). The structural evolution of the Fyfe Hills–Khmara Bay region, Enderby Land, east Antarctica. *Australian Journal of Earth Sciences* **31**, 403–426.

Schreyer, W. & Seifert, F. (1969). Compatibility relations of the aluminium silicates in the systems $MgO–Al_2O_3–SiO_2–H_2O$ and $K_2O–AlgO–Al_2O_3–SiO_2–H_2O$ at high pressures. *American Journal of Science* **267**, 371–388.

Sheraton, J. W. & Black, L. P. (1983). Geochemistry of Precambrian gneisses: relevance for the evolution of the East Antarctic Shield. *Lithos* **16**, 273–296.

Sheraton, J. W., England, R. N. & Ellis, D. J. (1982). Metasomatic zoning in sapphirine-bearing granulites from Antarctica. *BMR Journal of Geology & Geophysics* **7**, 269–273.

Sheraton, J. W., Tingey, R. J., Black, L. P., Offe, L. A. & Ellis, D. J. (1987). Geology of an unusual Precambrian high-grade metamorphic terrane—Enderby Land and western Kemp Land, Antarctica. *Australian Bureau of Mineral Resources Bulletin* **223**, 51 pp.

Spear, F. S. (1993). *Metamorphic Phase Equilibria and Pressure–Temperature–Time Paths. Mineralogical Society of America, Monograph*, pp. 608–625.

Thost, D. E. & Hensen, B. J. (1992). Gneisses of the Porthos and Athos Ranges, northern Prince Charles Mountains, constraints on the prograde and retrograde *P–T* path. In: Yoshida, Y., Kaminuma, K. & Shiraishi, K. (eds) *Recent Progress in Antarctic Earth Science*. Tokyo: Terra, pp. 93–102.

Vry, J. K. (1994). Boron-free kornerupine from the Reynolds Range, Arunta Block, central Australia. *Mineralogical Magazine* **58**, 27–37.

Waters, D. J. (1986). Metamorphic history of sapphirine-bearing and related magnesian gneisses from Namaqualand, South Africa. *Journal of Petrology* **27**, 541–565.

Waters, D. J. & Moore, P. B. (1985). Kornerupine in Mg–Al-rich gneisses from Namaqualand, South Africa: mineralogy and evidence for late-metamorphic fluid activity. *Contributions to Mineralogy and Petrology* **91**, 247–259.

Wegge, S. & Schreyer, W. (1994). Boron-free kornerupine: its upper pressure stability limit in the system $MgO–Al_2O_3–SiO_2–H_2O$ (MASH). *European Journal of Mineralogy* **6**, 67–75.

Werding & Schreyer, W. (1996). Experimental studies on borosilicates and selected borates. In: Grew, E. S. & Anovitz, L. M. (eds) *Boron: Mineralogy, Petrology and Geochemistry. Mineralogical Society of America, Reviews in Mineralogy* **33**, 117–159.

Windley, B. F., Ackermand, D. & Herd, R. K. (1984). Sapphirine/kornerupine-bearing rocks and crustal uplift history of the Limpopo belt, Southern Africa. *Contributions to Mineralogy and Petrology* **86**, 342–358.

Young, D. N. & Black, L. P. (1991). U–Pb zircon dating of Proterozoic igneous charnockites from the Mawson coast, east Antarctica. *Antarctic Science* **3**, 205–216.

Young, D. N., Zhao, J.-X., Ellis, D. J. & McColloch, M. T. (1997). Geochemical and Sr–Nd isotopic mapping of source provinces for the Mawson charnockites, east Antarctica: implications for

Proterozoic tectonics and Gondwana reconstruction. *Precambrian Research* **86**, 1–19.

Zhao, J.-x., Ellis, D. J., Kilpatrick, A. & McColloch, M. T. (1997). Geochemical and Sr–Nd isotopic study of charnockites and related rocks in the northern Prince Charles Mountains, East Antarctica: implications for charnockite petrogenesis and Proterozoic crustal evolution. *Precambrian Research* **81**, 37–66.

REFERENCES IN SUPPLEMENTARY TABLES NOT CITED IN THE TEXT

Bhattacharya, A., Krishnakumar, K. R., Raith, M. & Sen, S. K. (1991). An improved set of *a–X* parameters for Fe–Mg–Ca garnets and refinements of the orthopyroxene–garnet thermometer and the orthopyroxene–garnet–plagioclase–quartz barometer. *Journal of Petrology* **32**, 629–656.

Bohlen, S. R., Wall, V. J. & Boettcher, A. L. (1983*a*). Experimental investigation and application of garnet granulite equilibria. *Contributions to Mineralogy and Petrology* **83**, 52–61.

Bohlen, S. R., Wall, V. J. & Boettcher, A. L. (1983*b*). Experimental investigations and geological applications of equilibria in the system FeO–TiO_2–Al_2O_3–SiO_2–H_2O. *American Mineralogist* **68**, 1049–1058.

Carswell, D. A. & Harley, S. L. (1989). Mineral thermometry and barometry. In: Carswell, D. A. (ed.) *Eclogite Facies Rocks*. Glasgow: Blackie, pp. 83–110.

Eckert, J. O., Newton, R. C. & Kleppa, O. J. (1991). The *H* of reaction and recalibration of garnet–pyroxene–plagioclase–quartz geobarometers in the CMAS system by solution calorimetry. *American Mineralogist* **76**, 148–160.

Harley, S. L. (1984). An experimental study of the partitioning of Fe and Mg between garnet and orthopyroxene. *Contributions to Mineralogy and Petrology* **86**, 359–373.

Lee, H. Y. & Ganguly, J. (1988). Equilibrium compositions of coexisting garnet and orthopyroxene—experimental determinations in the system FeO–MgO–Al_2O_3–SiO_2, and applications. *Journal of Petrology* **29**, 93–113.

Moecher, D. P., Essene, E. J. & Anovitz, L. M. (1988). Calculation and application of clinopyroxene–garnet–plagioclase–quartz geobarometers. *Contributions to Mineralogy and Petrology* **100**, 92–106.

Newton, R. C. & Perkins, D. (1982). Thermodynamic calibration of geobarometers based on the assemblages garnet–plagioclase–orthopyroxene (clinopyroxene)–quartz. *American Mineralogist* **67**, 203–222.

Wood, B. J. (1974). The solubility of alumina in orthopyroxene coexisting with garnet. *Contributions to Mineralogy and Petrology* **46**, 1–15.